THE EFFECT OF ENERGY INPUT ON FLOTATION KINETICS IN AN OSCILLATING GRID FLOTATION CELL

By

Kudzai Changunda

B.Sc. (Hon) Chemical Engineering

A thesis submitted to the

UNIVERSITY OF CAPE TOWN

in fulfilment of the requirements for the degree

MASTER OF SCIENCE IN ENGINEERING

Centre for Minerals Research

University of Cape Town

October 2012

Declaration

I know the meaning of plagiarism and declare that all the work in the document, save for that which is properly acknowledged, is my own.

Signed by candidate

Signature Removed

Kudzai Changunda

22 October 2012

Acknowledgements

I would like to thank my supervisor, Professor David Deglon, and co-supervisor, Martin Harris, for their guidance, constant support and patience. Thank you for the invaluable insights and input, and keeping the project interesting.

I would also like thank and acknowledge the following:

- Thank you to the University of Cape Town and the AMIRA P9N project for funding this research and the continued interest in the project.
- To Joachim Macke, Bill Randall and Granville de la Cruz for assisting with the construction of the oscillating grid cell used in this study.
- The entire Centre for Minerals Research (staff and students) for providing a stimulating and fun environment for learning and growing.
- To my manager, Lourens Havenga, for allowing me the time to concentrate on the thesis
- My fiancée, Nomsa, for her wonderful support and patience throughout the study.
- My parents and brothers for the continuous encouragement

Publications

Journal Publication

- Changunda, K., Deglon, D.A. and Harris. M. 2008. Investigating the effect of energy on flotation kinetics using a novel oscillating grid cell. International Journal of Minerals Engineering, 21, pp 924-929

Conference

- Deglon, D.A., Changunda, K. and Harris. M. 2007. Investigating the effect of energy on flotation kinetics using a novel oscillating grid cell., *Flotation 07*. Cape Town., South Africa

SYNOPSIS

Energy is known to play an important role in particle-bubble contacting in flotation. This thesis investigates the effect of energy input (or agitation) on the flotation kinetics of quartz in a novel oscillating grid flotation cell. The effects of bubble size and particle size have been recognized as important variables affecting particle-bubble contacting in turbulent systems and are investigated in this thesis.

The research work done in this thesis is a continuation of the work done by the Centre for Minerals Research by Deglon (1998) who investigated the effects of energy in a batch mechanical flotation cell. However, this system has a very complex hydrodynamic environment, resulting from the large disparities in turbulence intensity. Previously Breytenbach (1995) had constructed a hybrid flotation column cell, which was essentially a column flotation cell that could be modified into a Jameson cell or a mechanically agitated column cell. He used this to compare particle collection efficiency in these different particle-bubble contacting environments. The third phase of the work was the oscillating baffle column (OBC), a novel flotation column that attains agitation by oscillating a set of orifice baffles through the slurry, thereby producing a more uniform shear rate distribution than would be obtained in an impeller driven system (Anderson, 2008). The OBC unfortunately has significant oscillatory flow and has high shear rates, which often result in detachment effects becoming appreciable.

Oscillating grids generate near ideal hydrodynamic environments, characterised by turbulence that is relatively homogeneous and isotropic. The oscillating grid flotation cell used in this study was based on the oscillatory multi-grid mixer used by Bache and Rasool (2001). The oscillatory multi-grid mixer was purchased from these authors and retrofitted to produce the oscillating grid flotation cell. The novel oscillating grid cell consists of a 10 litre tank agitated by 19 grids with a mesh size of 8 mm and grid spacing of 18 mm.

The grids were oscillated at a fixed amplitude, equal to the grid spacing, and over a range of frequencies, using a variable speed drive. Frother was added at 100 ppm to be consistent with the work of Deglon (2002) and Ahmed and Jameson (1985). A low gas flow-rate (100 ml/min) and solids concentration were specifically chosen in order that there was minimal influence on the structure of turbulence in the oscillating grid cell, as Bache and Rasool (2001) took measurements in water. Flotation tests were performed on methylated quartz particles (P_{80} = 100 μm) over a range of power intensities (0.015–0.60 W/kg) and using three different bubble sizes, generated by sintered glass discs (0.13, 0.24 and 0.82 mm).

The flotation rate constant was found to increase approximately linearly with increasing particle size for all three bubble sizes. This was due to the increased probability of collision for larger particles and is well established in the flotation literature. A number of researchers have found that the flotation rate constant for quartz particles increases almost linearly with particle size, at low power intensities. An inverse power relationship was observed between bubble size and flotation rate constant for all fine, middling and coarse particle size ranges. This inverse power relationship was due to the increased probability of collision for smaller bubbles and is also well established in the flotation literature.

More significantly, the flotation rate constant was found to increase almost linearly with increasing power intensity for all particle and bubble sizes used in this study. The majority of theoretical and experimental studies have found energy input to have less of an effect than the proportional/linear dependence observed in this study. In addition, the increase in the flotation rate constant with increasing power intensity was observed to depend on particle size, but to be less dependent on bubble size. These findings suggest that energy input and bubble size may respectively play more and less of a role in promoting particle–bubble contacting in turbulent environments than was noted in the flotation literature. However, a recent study by Newell and Grano (2006) done using a stirred tank also noted this linear dependence.

Given the findings of this thesis, it is strongly recommended that further work be done to investigate the OGC at higher energy intensities (~3W/kg) and to scale it up so that it can be more comparable to the widely used mechanical flotation cells. The homogeneous and nearly

isotropic turbulence generated by the OGC also makes it an ideal environment to characterize floatability for different ores.

TABLE OF CONTENTS

SYNOPSIS ..... **I**

TABLE OF CONTENTS ..... **IV**

LIST OF FIGURES ..... **VIII**

LIST OF TABLES ..... **X**

NOMENCLATURE ..... **XI**

CHAPTER 1 : INTRODUCTION **1**

1.1 BACKGROUND 1

1.2 PROBLEM STATEMENT 2

1.3 SCOPE AND OBJECTIVES 2

CHAPTER 2 : LITERATURE REVIEW **4**

2.1 FROTH FLOTATION 4

2.1.1 Overview of flotation 4

2.1.2 Sub-processes of flotation 5

2.1.2.1 Conditioning 6

2.1.2.2 Particle collection 6

2.1.2.2.1 Collision 7

2.1.2.2.2 Attachment 7

2.1.2.2.3 Detachment 8

2.1.2.3 Froth removal 8

2.1.3 Overview of flotation cells 9

2.1.3.1 Mechanical flotation cells 9

2.1.3.2 Column flotation cells 9

2.1.3.3 Novel flotation cells 10

2.2 PARTICLE HYDROPHOBICITY 10
2.2.1 Ideal surfaces and particles 10
2.2.2 Non-ideal surfaces and particles 13
2.3 TURBULENCE 14
2.4 EFFECT OF ENERGY/AGITATION ON FLOTATION KINETICS 17
2.4.1 Theoretical findings 18
2.4.1.1.1 Brownian motion 20
2.4.1.1.2 Shear mechanism 20
2.4.1.1.3 Accelerative method 21
2.4.1.1.4 Purely accelerative mechanism 22
2.4.1.1.5 Intermediate correlations 23
2.4.1.1.6 Velocity correlations for collision frequency 25
2.4.2 Experimental findings 27
2.5 GRID AGITATION 28
2.5.1 Single-grid systems 28
2.5.2 Two grid systems 36
2.5.3 Multi-grid systems 38
2.5.3.1 Description of the multi-grid mixer 38
2.5.3.2 Turbulence characteristics 39
2.5.3.3 Power characterisation 41
2.6 THE EFFICACY OF THE MULTI-GRID MIXER AS A FLOTATION RESEARCH TOOL 42
CHAPTER 3 EXPERIMENTAL 43
3.1 THE OSCILLATING GRID FLOTATION CELL 43
3.1.1 The flotation tank 44
3.1.2 The grid mixing system 45
3.1.3 Aeration and froth removal system 46
3.2 PRE-CHARACTERISATION EXPERIMENTS 47
3.2.1 Particle sizing 47
3.2.2 Methylation of quartz 49

3.2.3 Contact angle measurement 49
3.2.4 Bubble size determination 52
3.3 FLOTATION EXPERIMENTS 52
3.3.1 Experimental conditions 53
3.3.1.1 Oscillating amplitude/stroke 53
3.3.1.2 Choice of reagents 53
3.3.1.3 Air flow-rate and pulp density 53
3.3.2 Experimental variables 54
3.3.2.1 Power input and frequency 54
3.3.3 Experimental procedure 54
3.4 HYDRODYNAMIC CHARACTERISATION OF THE CELL 55
CHAPTER 4 : RESULTS AND DISCUSSION 57
4.1 PRECHARACTERISATION 58
4.1.1 Flotation recovery 58
4.1.2 Reproducibility 59
4.1.3 Kinetic analysis 60
4.1.3.1 Modelling 60
4.1.3.2 Entrainment 60
4.2 EFFECT OF PARTICLE AND BUBBLE SIZE 62
4.2.1 Effect of particle size on flotation rate constant 62
4.2.2 Effect of bubble size on the flotation rate constant 64
4.3 EFFECT OF ENERGY 66
4.3.1 Effect of power intensity on the flotation rate constant 66
4.3.2 Absolute effect of power intensity on the flotation rate constant 68
4.3.3 Summary of findings 70
CHAPTER 5 CONCLUSIONS AND RECOMMENDATIONS 71
5.1 CONCLUSIONS 71
5.2 RECOMMENDATIONS FOR FUTURE WORK 72

REFERENCES 73

APPENDIX 81

A1: FLOTATION RECOVERY DATA 81

Recovery-by-size for 0.13 mm bubbles (Run 1) 81
Recovery-by-size for 0.13 mm bubbles (Run 2) 82
Recovery-by-size for 0.24 mm bubbles 82
Recovery-by-size for 0.82 mm bubbles 83

A2: FLOTATION RATE CONSTANTS (BUBBLE SIZE = 0.82 MM) 85

A3: FLOTATION RATE CONSTANTS (BUBBLE SIZE = 0.24 MM) 85

A4: FLOTATION RATE CONSTANTS (BUBBLE SIZE = 0.13 MM) 85

LIST OF FIGURES

Figure 2.1. Schematic representation of the flotation process in a mechanical cell. 5

Figure 2.2. Schematic representation of froth flotation sub-processes (Deglon, 1998). 6

Figure 2.3. Contact angle (θ) of gas bubble in water on a solid surface..... 11

Figure 3.1. The oscillating grid flotation tank. 43

Figure 3.2. Schematic diagram of the flotation tank. 44

Figure 3.3. Schematic diagram of the grid mixing system. 45

Figure 3.4. Flow diagram of the flotation aeration system. 46

Figure 3.5. Flow diagram of the froth removal system..... 47

Figure 3.6. Quartz particle size distribution in the flotation feed 48

Figure 3.7. Experimental apparatus used for determining the contact angle of particles, as described by Washburn (1921). 50

Figure 3.8. Wetting kinetics for -106 µm hydrophobic quartz 51

Figure 3.9. Graph of RMS turbulent velocity (dimensionless) versus column height (mm) for a grid frequency of 2.05 Hz. Adapted from Bache and Rasool (2001). 56

Figure 4.1. Graph showing the relationship between particle size (µm) and recovery (%) for 0.13 mm bubbles after 8 minutes (ε = 0.44 W/kg). 58

Figure 4.2. Recovery-time curves for three particle size ranges and for three repeat flotation tests (ε = 0.58 W/kg, 0.13 mm bubbles). 59

Figure 4.3. Water recovery-time curves for four different energy levels. 61

Figure 4.4. Graph of flotation rate constant (min^{-1}) versus particle size (µm) for three bubble sizes (ε = 0.15 W/kg). 62

Figure 4.5. Graph of flotation rate constant (min^{-1}) versus particle size (µm) for three bubble sizes (ε = 0.44 W/kg). 63

Figure 4.6. Graph of flotation rate constant (min^{-1}) versus bubble size (mm) for three particle size ranges (ε = 0.15 W/kg)..... 64

Figure 4.7. Graph of flotation rate constant (min^{-1}) versus bubble size (mm) for three particle size ranges (ε = 0.44 W/kg)..... 65

Figure 4.8. Graph of flotation rate constant (min-1) versus power intensity (W/kg) for the -10.5 + 4.9 µm particle size range. 66

Figure 4.9. Graph of flotation rate constant (min-1) versus power intensity (W/kg) for the -48.3 + 26.2 µm particle size range for different bubble sizes. 67

Figure 4.10. Graph of flotation rate constant (min^{-1}) versus power intensity (W/kg) for the -76.3 + 48.3 µm particle size range for different bubble sizes..... 67

Figure 4.11. Graph showing increase in flotation rate constant (min^{-1}) versus power intensity (W/kg) for three particle size ranges..... 69

LIST OF TABLES

Table 2.1. Collision mechanism in turbulence..... 19

Table 2.2. Table showing the different values for constants C_1 and C_2..... 30

Table 3.1. Particle size analysis of the feed fraction, as given by the Malvern Mastersizer 48

Table 3.2. Mean, Sauter mean and percentile bubble size as measured by Deglon (1998)..... 52

Table 3.3. The experimental conditions and variables used for the experiments..... 53

Table 4.1 Recovery and rate constants and their relative errors per size class (ε = 0.58 W/kg, 0.13 mm bubbles)..... 60

NOMENCLATURE

P_{80}	80% passing particle sizes
P_c	Probability of collision
d_p	Particle diameter
d_b	Bubble diameter
γ_{sv}	Solid-air interfacial tension
γ_{sl}	Solid-liquid interfacial tension
γ_{lv}	Liquid-air interfacial tension
Θ	Static contact angle
θ_a	Advancing contact angle
θ_r	Receding contact angle
R_1 , R_2	Two principal radii of curvature
ΔP	Pressure difference across the interface
W_F	Downward force
P	Density
H	Height the fluid rises
r_{eff}	Capillary radius
$\Delta\rho$	Difference in density
μ	Viscosity
T	Time
$u(t)$	Turbulent fluctuation velocity component
u_{rms}	Root-mean-squared fluctuating velocity
η	Kolmogorov length scale
τ_k	Kolmogorov time scale
Z_{ij}	Collision frequency
T	Absolute temperature

k_b	Boltzmann constant
r_i , r_j	Radii of colliding particles and/or bubbles
d_i , d_j	Diameter of colliding particles and/or bubbles
St	Stokes number
τ_i	Particle relaxation time
v_{ps}	Particle settling velocities
v_b	Bubble rise velocities
T_L	Langragian integral time scale
θ_i	Dimensionless relaxation time
M	Grid mesh size
S	Grid amplitude/stroke
F	Grid frequency
Z	Distance from the mid plane of the oscillating grid
C_1 , C_2	Oscillating grid tank-geometry dependent constants
L	Turbulent integral scale
$q^2/2$	Mean kinetic energy per unit mass
$\phi(f)$	Kinetic energy per unit frequency
P	Measured power input
A	Plan area of grid
σ	Grid solidity
m_L	Mass of liquid in system
D	Grid diameter
τ_E	Eulerian integral time scale
$R(t)$	Autocorrelation function
$E(f)$	Fitted power spectra generalized distribution function
$\sigma_k, \sigma_\varepsilon$	Constants for k - ε model
C_2 , C_μ	Constants for k - ε model
l_t	Characteristic lengthscale of k - ε model

H	Distance between the two grids
U^2	Average velocity intensity per component
C_p	Calibration constant
R_N	Grid Reynolds number
n_g	Number of grids
P_1	Energy input per grid

CHAPTER 1 : INTRODUCTION

1.1 Background

Although mining contributes significantly to South Africa's energy supply, through the production of coal and synthetic fuels, it is also recognized that the industry demands a great deal of the country's energy. The Department of Minerals and Energy (DME) estimates that the mining industry accounts for 6% of overall energy consumption in South Africa. The DME has set a 15% energy demand reduction target for the mining sector, to be met by 2015. In order to meet the current mandates of sustainable development in this industry, research plays an increasingly crucial role in identifying future methods that will be implemented to ease the energy burden and environmental concerns, while maintaining productivity.

The research work done here is a continuation of the work done at the Centre for Minerals Research (Deglon, 1998), which investigated the effects of energy in a batch mechanical flotation cell. However, this system has a very complex hydrodynamic environment, resulting from the large disparities in turbulence intensity. Previously, Breytenbach (1995) had constructed a hybrid flotation column cell, which was essentially a column flotation cell that could be modified into a Jameson cell or a mechanically agitated column cell. He used this to compare particle collection efficiency in these different particle-bubble contacting environments. The third phase of the work was the oscillating baffle column (OBC), a novel flotation column that attains agitation by oscillating a set of orifice baffles through the slurry, thereby producing a more uniform shear rate distribution than would be obtained in an impeller driven system (Anderson, 2008). The OBC unfortunately has significant oscillatory flow and has high shear rates, which often result in detachment effects becoming appreciable.

This study investigates the effect of energy input on the flotation kinetics of methylated quartz particles in a novel oscillating grid flotation cell. This cell is another form of an agitated column, which uses grids that oscillate vertically to create mixing. The oscillating grid cell has more

variables (frequency and stroke) than a mechanical cell, resulting in better control of the hydrodynamic environment. The removable gas frits allow for fine bubble generation more suited to fine particle flotation. Above all, oscillating grids generate near ideal hydrodynamic environments, characterized by turbulence that is relatively homogeneous and isotropic at low energy. To the author's knowledge, this thesis is one of the first studies in which flotation tests have been conducted in a near ideal turbulent environment.

1.2 Problem Statement

There is a need to understand the effect of energy on flotation in an ideal hydrodynamic environment with near homogeneous and isotropic turbulence in order to optimize its use in flotation.

Energy plays an important role in particle-bubble contacting. A number of excellent studies have attempted to address this issue by investigating flotation kinetics in standard stirred tanks, agitated by Rushton turbine impellers (Ahmed and Jameson, 1985; Deglon, 2002; Pyke *et al.*, 2003; Newell and Grano, 2006). These vessels have well-defined hydrodynamic environments, but are characterized by turbulence that is strongly inhomogeneous throughout the vessel and may be anisotropic in the impeller zone. This complicates investigation of the effect of energy input on flotation kinetics as particle-bubble contacting is considered to be driven by turbulence, with many flotation theories/models based on the assumption of homogeneous, isotropic turbulence.

1.3 Scope and Objectives

The primary objective of this thesis was to investigate the effect of energy on flotation in an ideal environment with near homogeneous and isotropic turbulence and with uniform energy dissipation throughout the fluid. The effects of bubble size and particle size have been recognized as important variables affecting particle-bubble contacting in turbulent systems and will be investigated in this study. Three variables have been chosen, namely: energy, particle size and bubble size.

The experiments were designed such that the primary objective is to determine the effect of energy on the flotation process in a nearly ideal system in terms of turbulence and energy

dissipation. The effect of energy was investigated by changing the frequency at which the grids oscillate using a variable speed drive. Five different frequency settings were chosen to cover the energy range (0.015 – 0.60 W/kg) investigated. This is similar to changing the impeller speed in an industrial or laboratory impeller driven cell.

A normally distributed sample of quartz with 80% passing 100 μm particles, was used for the experiments. It allowed investigation of fine particle flotation (sub 10 μm) and the entire particle size range, as indicated in Figure 3.6. Three different bubble sizes, namely 0.13 mm, 0.24 mm and 0.82 mm, were also investigated in order to determine a relationship between bubble size and flotation rate in this hydrodynamic system.

CHAPTER 2 : LITERATURE REVIEW

This chapter gives an overview of the literature relevant to this thesis. Section 2.1 gives an overview of froth flotation. Contact angle measurement was an important part of the characterisation of the methylated quartz particles and as such hydrophobicity is discussed in Section 2.2. A brief overview of turbulence is presented in Section 2.3. Section 2.4 discusses the various theoretical and experimental studies done previously by other researchers on determining the effect of energy on flotation kinetics. Agitation using grids is then discussed in Section 2.5 and, finally, the effectiveness of the grid mixer is examined in Section 2.6.

2.1 Froth flotation

2.1.1 Overview of flotation

Froth flotation is the most widely used beneficiation method in the mineral processing industry. It is an important process used to recover minerals, such as gold, platinum, copper and other base metals. It is a mineral recovery sub-process that uses particle hydrophobicity or hydrophilicity to separate the mineral from the unwanted material. Hydrophobic particles are attached to air bubbles and form particle-bubble aggregates that rise to the froth layer while the hydrophilic particles remain in the pulp zone (see Figure 2.1).

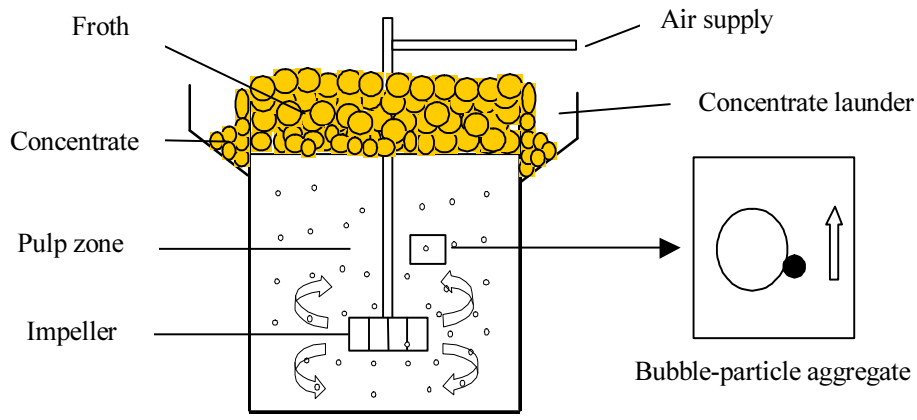

Figure 2.1. Schematic representation of the flotation process in a mechanical cell.

Flotation has allowed low-grade ores, or ores containing finely disseminated minerals that would otherwise have been uneconomic, to be treated. Originally used to treat lead, zinc and copper sulphide ores, froth flotation is now applied to over one hundred different minerals, including iron oxides, oxidised minerals such as malachite and non-metallic ores such as coal.

2.1.2 Sub-processes of flotation

In order for the froth flotation process to be successful, a number of sub-processes need to occur, as can be seen in Figure 2.2. These are reviewed under the three broad terms identified by Schulze (1984): conditioning, particle collection and froth removal. The following review has been summarized from the comprehensive reviews done by Deglon (1998) and Lewis (2003).

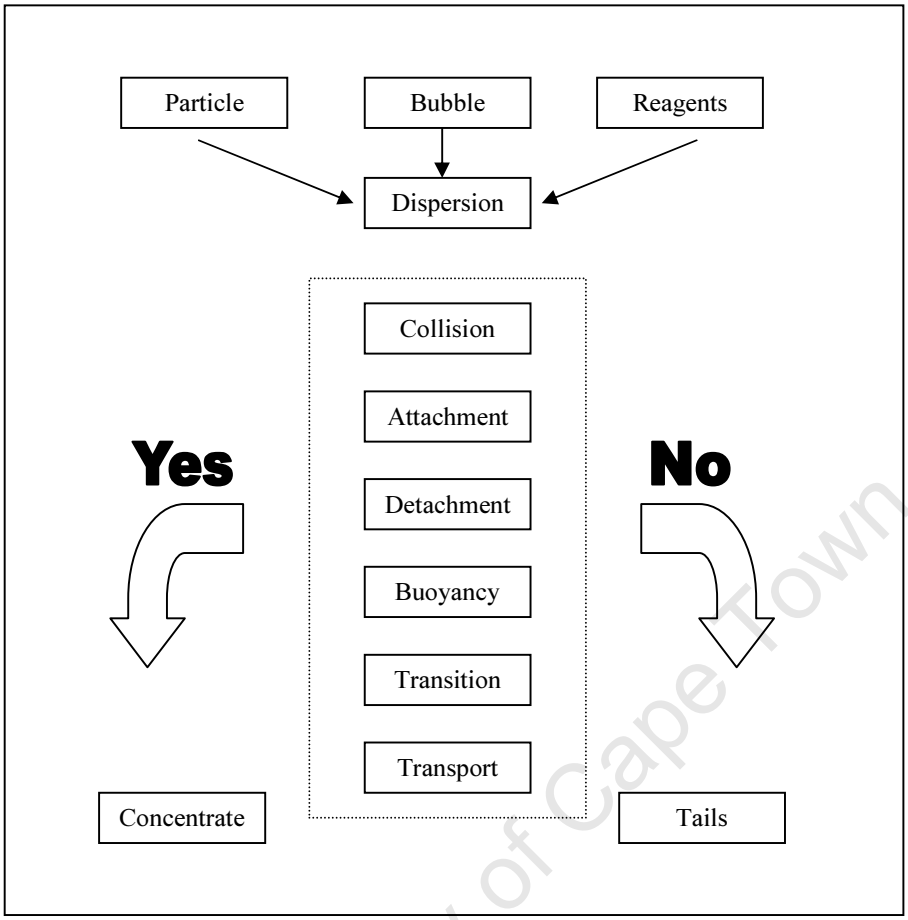

Figure 2.2. Schematic representation of froth flotation sub-processes (Deglon, 1998).

2.1.2.1 Conditioning

Reagents such as collectors, frothers, activators and depressants are added to the cell with suspended solid particles in the form of slurry. Collectors are used to render the surface of the valuable mineral hydrophobic, and therefore amenable to collection. Frothers are used to aid in bubble formation and froth stabilisation at the surface of the cell. Depressants are used to suppress flotation of naturally hydrophobic gangue minerals in the slurry.

2.1.2.2 Particle collection

After an appropriate conditioning time, air is introduced into the flotation cell. Collision, attachment and detachment sub-processes are extremely important to flotation, as they determine the overall success of the process, namely the ability to collect and remove valuable mineral

particles from the pulp. Hydrophobic mineral particles are contacted with gas bubbles via collision, and mineral particles adhere to the bubbles (attachment). Thereafter particle-bubble aggregates have to have sufficient buoyancy to rise through the pulp and be sufficiently stable to endure disturbance in the pulp that may cause detachment. These important sub-processes will be discussed in further detail in the sections that follow. When the particle-bubble aggregate reaches the pulp-froth interface, it leaves the collection zone and enters the froth zone where it is removed as concentrate while the hydrophilic particles remain in the pulp.

2.1.2.2.1 Collision

Collision is the process whereby hydrophobic and conditioned mineral particles are brought into contact with gas bubbles that are dispersed inside the flotation cell. The main mechanism of collision is a direct encounter between particle and bubble in suspension (Arbiter, 1999). To collide with a bubble, a solid particle must have sufficient momentum to resist the tendency to follow streamlines around the bubble (Ahmed and Jameson, 1989). Collision is commonly measured in terms of probability of collision (P_c), which is defined as the ratio of the number of particles encountering a bubble to the number of particles approaching a bubble in the flow tube of equivalent diameter. Many expressions exist for the probability of collision E_c, but one of the more common expressions is as per Equation 2.1 below:

$$P_c = \frac{d_p^m}{d_b^n} \tag{2.1}$$

where d_p is particle size, d_b is bubble size, and m and n vary between 1 and 3.

2.1.2.2.2 Attachment

Attachment of particles to bubbles is a complex interaction of both hydrodynamic and surface forces. The probability of attachment (P_a) is defined as the fraction of particles that remain attached to bubbles after collision has occurred. Once a collision has occurred, there are a number of micro-processes that need to occur for the particle to adhere to the bubble. Ahmed and

Jameson (1989) identified three micro-processes that occur during the attachment/adhesion of a particle to a bubble:

- Approach of a particle to a bubble.
- Thinning of the water film between particle and bubble to rupture thickness.
- Receding of the residual film to give an air-solid interface.

It is believed that the second step is the controlling mechanism in this process. Whether the particle can attach is dependent on the contact time between particle and bubble, τ_{con} (Schulze, 1984). During this contact period, the thin liquid film between the bubble and the particle must drain and rupture, giving a three-phase contact (TPC), which is large enough to stabilize the aggregate. Laskowski (1989) postulated that attachment of particles to bubbles has a probability that is dependent on a thermodynamic energy barrier, which is the result of long range forces between particles and bubbles acting at the moment of attachment.

2.1.2.2.3 Detachment

Detachment between particles and bubbles may occur if conditions in the cell make the particle-bubble aggregate unstable, resulting in the mineral particle becoming separated from the bubble and returning to the pulp. The probability of detachment is defined as the fraction of attached particles that detach from bubbles in the flotation cell. This is controlled by both the stability of particle-bubble aggregates and external shear stresses in the cell.

2.1.2.3 Froth removal

If a particle-bubble aggregate survives detachment in the collection zone, it crosses over the pulp-froth interface into the froth phase. Within this froth phase are mineral-loaded bubbles and entrained hydrophilic (gangue) particles together with the hydrophobic particles that may have detached from the bubbles in the froth. These are removed as the flotation concentrate.

2.1.3 Overview of flotation cells

Mechanical flotation cells and column flotation cells are by far the most widely used in the flotation industry. This overview has been adapted from Deglon (1998) and Anderson (2008).

2.1.3.1 Mechanical flotation cells

Mechanical flotation cells are large tanks up to 300 m^3 in volume that are agitated by an impeller with power input between 1 – 3 kW/m^3. Mechanical cells use a large mixer and diffuser mechanism at the bottom of the mixing tank to introduce air and provide the mixing action. These are the most widely used cells in the flotation industry. However, flotation optimization in a mechanical cell is difficult because the impeller is responsible for gas dispersion, solid suspension and particle–bubble contacting. There are also large energy and turbulence disparities in this kind of system, making the hydrodynamic environment very complex.

2.1.3.2 Column flotation cells

Column flotation cells are usually tall cylindrical columns up to 15 m high and 3 m diameter. The fresh feed, in the form of slurry, is fed near the top of the cell, whilst the gas bubbles are sparged at the bottom of the cell, hence achieving quiescent counter-current contacting. Column flotation cells decouple the three sub-processes - gas dispersion, solid suspension and particle–bubble contacting - which results in improved operation and control. In addition, because they allow deep froth formation, they are capable of producing high grade product. Unfortunately, large particles have a high settling velocity, resulting in a shorter residence time. This makes them difficult to recover. Fine particles cannot overcome the streamlines around the bubble. This makes them less likely to collide with bubbles. Agitated columns were a first attempt at improving fine particle flotation in column flotation cells. These flotation cells often exist with a series of impellers down the length of the columns to improve contacting. However, sophisticated control systems are required because of their high aspect ratios.

2.1.3.3 Novel flotation cells

Numerous novel flotation cells have been developed since the inception of the flotation process. All have been developed in an attempt to exploit or improve the various sub-processes of flotation. These improvements have been largely instigated by a better understanding of flotation fundamentals, which has led to an appreciation of the microenvironment necessary for optimizing flotation performance.

2.2 Particle hydrophobicity

Mineral particles have to be hydrophobic in order to be floatable under normal flotation conditions. Hydrophobicity is defined as the property of being water-repellent or as the ability of a solid surface to repel water. It is often characterised by the contact angle (θ) between the solid and liquid phases at the interface. In flotation, contact angles lie between 0˚ - 90˚, with 0˚ – 30˚ being low hydrophobicity, 30˚ - 70˚ being intermediate hydrophobicity and 70˚ – 90˚ being high hydrophobicity. The techniques employed to determine the contact angle are divided into two groups: ideal particle contact angle measurement; and non-ideal contact angle measurement, which will be dealt with separately. Sub-sections 2.2.1 and 2.2.2 are reviews of a paper by Chau (2009) on the techniques for measuring contact angles on mineral surfaces.

2.2.1 Ideal surfaces and particles

Figure 2.3 below illustrates the contact angle of a bubble on a mineral surface in an aqueous medium. By resolving the three interfacial tensions - solid-air γ_{sv}, solid-liquid γ_{sl} and liquid-air γ_{lv} - the equilibrium relation known as Young's equation (King, 1982) is obtained, as shown in Equation 2.2 below:

$$\gamma_{sv} = \gamma_{sl} + \gamma_{lv} \cos\theta \qquad (2.2)$$

where θ is the static contact angle.

Young's equation is only valid for surfaces that are smooth, flat, homogeneous, inert, insoluble, non-reactive, non-porous and non-deformable. There exist different techniques to measure the

contact angle and the value obtained from these different methods lies somewhere between the advancing angle (θ_a) and the receding angle (θ_r).

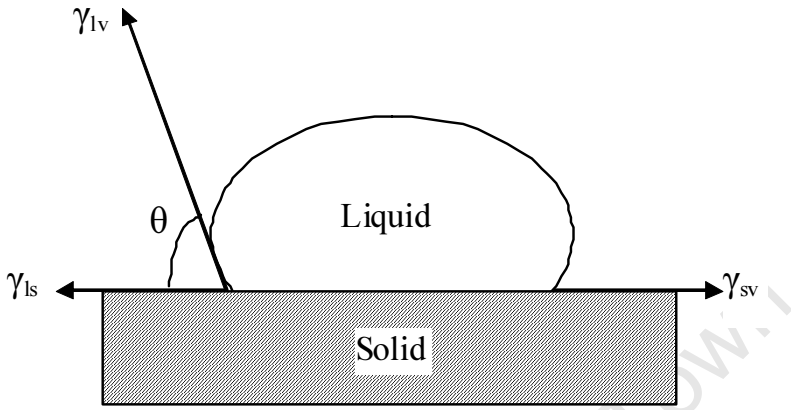

Figure 2.3. Contact angle (θ) of gas bubble in water on a solid surface

Drop profile: This method involves direct measurement of the contact angle by viewing the drop profile. A protractor is used to measure the contact angle on a traced outline of an image of the drop or adhering bubble projected onto a screen or photograph: Bigelow *et al.* (1946) used a telescope goniometer; Leja and Poling (1960) used a photograph, which can be taken for permanent record. Another form of this measurement is known as the captive-bubble method, developed by Taggart *et al.* (1930): the bubble is placed above the mineral surface (as opposed to under it) and is held by a glass holder.

Drop dimensions: These methods involve measurement of parameters that determine the entire profile of a drop resting on a surface. The shape of the symmetrical (axial) drop interface is described, starting with the Laplace equation below (Equation 2.3):

$$\gamma\left(\frac{1}{R_1}+\frac{1}{R_2}\right)=\Delta P \tag{2.3}$$

where: R_1 and R_2 are the two principal radii of curvature, as determined from a photograph of the drop; and ΔP is the pressure difference across the interface.

Fisher (1979) developed a theoretical expression that relates the contact angle to the radius and the volume, which is used in conjunction with the numerical integration of the Laplace equation.

Axisymmetric drop shape analysis (ADSA) profiling is a technique that was first developed by Rotenberg *et al.* (1983). The method fits the best Laplace shape using Equation 2.3 to the whole drop by using the interfacial tension as an adjustable parameter. However, the method assumes that gravitational force is the only external force and that the drop is symmetrical axially.

Wilhelmy method: This technique, developed by Wilhelmy (1863) is another form of the drop dimension technique that makes use of the perimeter of the line of contact (p) to determine the downward force (W_F) exerted on a thin smooth plate when it is brought into contact with a liquid (see Equation 2.4 below).

$$W_F = p\gamma_{lv}\cos\theta - V\Delta\rho g \tag{2.4}$$

where V is the volume and $\Delta\rho$ and the difference in densities

Capillary rise: A liquid rises when put in contact with a vertical plate. The height the fluid rises (h) can be determined by applying the Laplace equation to yield:

$$\sin\theta = 1 - \left(\frac{\Delta\rho g h^2}{2\gamma_{lv}}\right) \tag{2.5}$$

The contact angle can be obtained by measuring the capillary rise of the liquid up the plate (h). The combination of the capillary rise technique (Equation 2.5) and the Wilhelmy method (Equation 2.4) allows determination of the contact angle and the surface tension simultaneously.

However, all the above methods are only applicable on clean, smooth, flat homogeneous surfaces. In the context of flotation of real minerals, where the surface is irregular in terms of shape and morphology, such measurements are either impossible or non-representative of the entire mineral. The section below considers contact angle measurements of non-ideal surfaces and particles.

2.2.2 Non-ideal surfaces and particles

Measurement of the contact angle of non-ideal surfaces and particles is certainly more useful and relevant to mineral flotation, where particles and surfaces are often irregularly shaped and non-homogeneous. An extension of the ADSA method described above, known as axisymmetric drop shape analysis-diameter (ADSA-D), provides accurate measurement of small contact angles on imperfect solid surfaces. The technique involves viewing the top view of a drop on a surface and obtaining the contact diameter of the drop, which, together with the liquid surface tension and the volume of the drop, can be used to calculate the contact angle via numerical integration of the Laplace equation (Equation 2.3)

However, the ADSA-D measurement cannot be considered representative of all minerals in the pulp. In addition, the particle size range of interest in flotation is 10 – 200 μm, which makes it impossible to apply the method. Methods that have been developed to determine hydrophobicity (wettability) of solids in packed beds are considered best for the flotation application.

The wetting rate measurement technique (also known as the Washburn technique) used by Schwarz (2004) is a dynamic method that utilizes the Washburn equation, i.e.:

$$\frac{h^2}{t} = \frac{r_{eff}^2}{8\mu l}\left(\frac{2\gamma_{lv}\cos\theta_p}{r_{eff}} - \Delta\rho gh\right) \tag{2.6}$$

where: μ is the viscosity of the penetrating liquid; r_{eff} is the capillary radius; Δρ is the difference in density between the liquid and surrounding medium; h is the height of the liquid penetrating the bed in time t; and θ_p is the liquid phase contact angle.

The Washburn equation relates the capillary driving force of a liquid through a packed bed of particles to viscous drag. For a vertical bed with small pore radius, Δρgh can be neglected, as indicated in Equation 2.7 below.

$$\frac{h^2}{t} = \frac{r_{eff}\gamma_{lv}\cos\theta_p}{2\mu} \tag{2.7}$$

If the rate of penetration of a perfectly wetting liquid (w) with a known contact angle of 0° (cos $\theta_p = 1$) with the mineral particles is measured, Equation 2.7 reduces to:

$$\cos\theta_w = 1 = \left(\frac{h^2}{t}\right)_w \frac{2\mu_w}{r_{eff}(\gamma_{lv})_w} \tag{2.8}$$

Likewise, if the liquid is non-wetting (nw), Equation 2.7 reduces to:

$$\cos\theta_{nw} = \left(\frac{h^2}{t}\right)_{nw} \frac{2\mu_{nw}}{r_{eff}(\gamma_{lv})_{nw}} \tag{2.9}$$

For a particular fixed packing in a column, the effective capillary radius, r_{eff}, will be constant and a plot of h^2 versus t will be linear. By dividing Equation 2.9 by Equation 2.8, the r_{eff} does not need direct calculation and the contact angle for the non-wetting liquid can be obtained (Schwarz, 2004; Subrahmanyam *et al.*, 1996):

$$\cos\theta_{nw} = \frac{(h^2/t)_{nw}(\gamma_{lv})_w\mu_{nw}}{(h^2/t)_w(\gamma_{lv})_{nw}\mu_w} \tag{2.10}$$

$$\cos\theta_{nw} = \frac{\text{gradient of non wetting liquid}}{\text{gradient of wetting liquid}} \times \frac{(\gamma_{lv})_w\mu_{nw}}{(\gamma_{lv})_{nw}\mu_w} \tag{2.11}$$

The technique therefore involves the measurement of the height of a rising liquid through a packed bed of particles contained in a capillary tube as a function of time.

2.3 Turbulence

Turbulence is a three-dimensional intermittent flow dominated by vertical motion usually associated with a large Reynolds number. It is a flow regime characterized by low momentum diffusion, high momentum convection and rapid variation of pressure and velocity in space and time due to large scale instabilities within the flow.

Turbulence creates fluctuations in velocity. If the flow is laminar then the velocity at all time is the average velocity. For turbulent flow, however, the velocity record includes both a mean and a turbulent component, as shown below:

$$v(t) = \bar{v} + u(t) \quad u_{rms} = \sqrt{\overline{u(t)^2}} \tag{2.12}$$

where: $\bar{v}$ represents the mean velocity; and u(t) represents the turbulent fluctuation component.

The mean velocity can be evaluated through integration over a certain time interval, which must be much longer than any turbulence time scale. The turbulence strength is thus defined as $u_{rms} = \sqrt{\overline{u(t)^2}}$, where rms stands for "root mean square". This definition will apply for all three dimensions of space. The fluctuating velocity is therefore used to determine the turbulent kinetic energy (TKE):

$$TKE = \frac{1}{2}\left(u_{rms,x}^2 + u_{rms,y}^2 + u_{rms,z}^2\right) \tag{2.13}$$

The spectral description of turbulence is the most convenient way to describe turbulence. It is a result of continual flux of energy from larger eddies to smaller eddies.

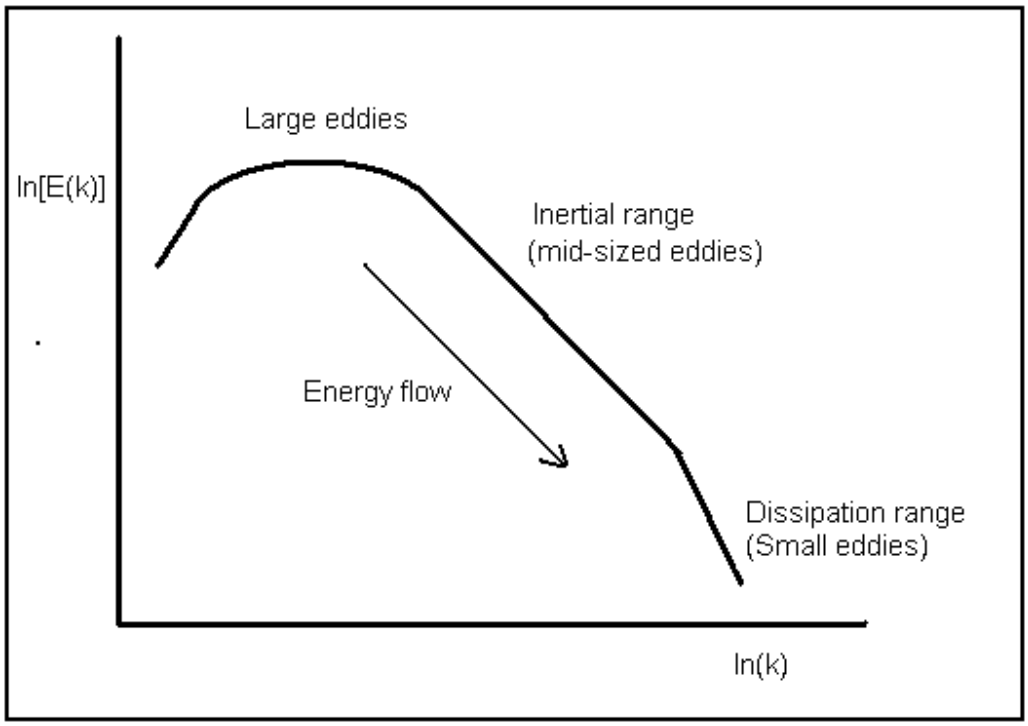

Figure 2.4. Turbulent energy spectrum. (k is the wave-number; E(k) is energy as a function of the wave-number)

The primary eddies, which are the largest, exist in the extreme left of the spectrum and are of similar scale to the turbulence generator. In the middle are mid-sized eddies, which have the most kinetic energy. These are the energy containing eddies. At the far right of the spectrum are small eddies, known as the inertial sub-range eddies and viscous dissipation eddies. These eddies transfer energy at a high rate relative to the rate at which the energy changes in these eddies. The inertial sub-range eddies are sufficiently small to be statistically independent of the bulk fluid and yet sufficiently large to transfer significant kinetic energy through inertial force. In the inertial sub-range, the net energy coming from the energy containing eddies is in equilibrium with the net energy cascading down to the viscous dissipation eddies, which have the least kinetic energy but which dissipate the most energy as heat. The collision process is considered of the scale of the inertial and viscous sub-range eddies. The primary and energy containing eddies are generally considered to be too large to influence the collision process and are responsible for bulk transport of particles.

Kolmogorov (1941) likewise predicted that energy is added at the highest turbulence scale and cascades down through the inertial scale to the dissipative scale (Kolmogorov microscale) without any energy being lost at any scale but the Kolmogorov microscale. This so-called Kolmogorov microscale is defined by

$$\eta = \left(\frac{\nu^3}{\varepsilon}\right)^{1/4} \tag{2.14}$$

$$\tau_k = \left(\frac{\nu^3}{\varepsilon}\right)^{1/2} \tag{2.15}$$

where η is the Kolmogorov length scale, τ_k is the Kolmogorov time scale. These are functions of the kinematic viscosity of the fluid (ν) and the energy dissipation (ε). Kolmogorov (1941) also characterized the intensity of micro-turbulence based on the size of the eddies:

$r_\theta \leq 12\eta$ laminar

$r_\theta \geq 12\eta$ to 15η turbulence

The above overview was derived from Hinze (1959), Deglon (1998) and Davidson (2003).

2.4 Effect of energy/agitation on flotation kinetics

Better, but still poor understanding of flotation fundamentals and flotation cell hydrodynamics has led to appreciation of the micro-environment and the effect of agitation on this environment. The effect of agitation on hydrodynamics, gas dispersion and particle–bubble contacting still remains poorly understood despite all the improvements. Energy is thought to increase the rate of flotation by increasing the number of particle-bubble collisions that occur. However there are limits of how much energy can improve the flotation process and the extent and rate to which energy improves flotation is largely uncertain. This section provides a review of the theoretical and experimental findings of the effect of agitation on the flotation process.

2.4.1 Theoretical findings

Agitation is considered to influence all of the sub processes of flotation, either directly or indirectly through bubble break-up and particle dispersion. Models for turbulent collision suggest that the rate of flotation is proportional to the specific power input (turbulent energy dissipation rate) to the power of between 0.50 and 0.75 (Deglon, 2002). The majority of theoretical studies suggest that agitation increases the rate of particle-bubble collision, which is especially important for fine particles (Saint Amand, 1999; Schubert, 1999). It is unclear whether agitation improves particle-bubble attachment due to conflicting results as to the effect of agitation on particle-bubble contact time. However, studies suggest that agitation helps to overcome the 'energy barrier' to attachment. All studies conclude that agitation significantly increases particle-bubble detachment for coarser particles but has a lesser influence on fine particles. Here, the destabilizing influence (probability of detachment, stress on aggregate, detachment force) has been shown to be proportional to the specific power input to the power of between 0.66 and 1.0 (Deglon, 2002). Several recent studies have combined the various theoretical models for particle-bubble collision, attachment and detachment in simulations of agitated flotation cells (Koh and Schwarz, 2003; Pyke *et al.*, 2003; Saint Amand, 1999). These studies demonstrate that agitation generally increases the rate of flotation of finer particles, as noted in numerous studies by Schubert (1999).

Table 2.1 gives the different correlations concerning modelling of collision frequency according to scale of turbulence. Since agitation/energy is thought to improve particle-bubble contacting by enhanced collision, the rest of this section reviews various collision models of relevance to turbulent collision.

Table 2.1. Collision mechanism in turbulence

Mechanism	Laminar/turbulent	Applicability
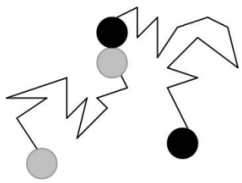 **Brownian Motion**	Laminar - very low turbulence	Particles must be less than 1 µm
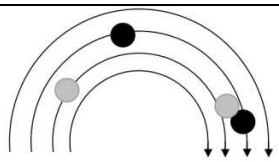 **Shear Mechanism**	Laminar and low turbulence	Particle and bubble smaller than smallest eddies – $(d_p + d_b) \ll \eta$
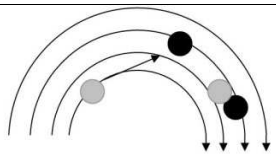 **Accelerative Mechanism**	Turbulent	Particle and bubble similar or smaller than smallest eddies - $(d_p + d_b) \leq \eta$
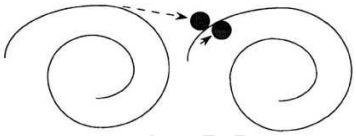 **Pure Accelerative Collision**	Highly Turbulent	Particles and bubbles are larger than smallest eddies - $(d_p + d_b) \geq \eta$ Particles and bubbles have independent velocities

2.4.1.1.1 Brownian motion

Brownian motion in flotation corresponds to particles colliding with bubbles due to their random Brownian motion and long range hydrophobic forces. This is more applicable to random movement of particles due to random movement of molecules in the environment and is considered to only have an effect on particle-bubble contacting for particles less than 1 μm. This is much smaller than the range of particle and bubble sizes encountered in flotation. Nonetheless, the Brownian model has been developed for very small particles in a very low turbulent environment. The collision frequency due to Brownian motion is thus given by (Smoluchowski, 1917) as indicated in Equation 2.16:

$$Z_{ij} = \frac{2k_b T}{3\mu}\left(\frac{1}{r_i} + \frac{1}{r_j}\right)\left(r_i + r_j\right) \tag{2.16}$$

where: k_b is the Boltzmann constant; T is absolute temperature; μ is the fluid viscosity and r_i, r_j is the radii of colliding particles and/or bubbles.

A recent study by Nguyen *et al.*(2006) showed that Brownian motion is only significant in sub-micron flotation for particles less than 0.1 μm. This further limits its application in most industrial and laboratory flotation applications.

2.4.1.1.2 Shear mechanism

The shear mechanism applies to laminar and low turbulence flow fields. Particles and bubbles follow streamlines within the viscous dissipation eddies range and collide due to their different positions within a shear flow field. Smoluchowski (1917) also developed an expression for the collision frequency for particle-particle collision in a shear flow field, i.e. Equation 2.17:

$$Z_{shear} = \frac{4}{3}\left(d_i + d_j\right)^3\left(\frac{du}{dy}\right) \tag{2.17}$$

where *du / dy* is the velocity gradient or shear rate in a laminar flow field for colliding particles and /or bubbles with diameter d_i and d_j.

Equation 2.17 only considers laminar flow with collisions caused by shear, whereby particles do not deviate from the fluid path. The tendency of particles to follow streamlines is characterized by the Stokes number (St), as indicated in Equation 2.18:

$$St = \frac{\tau_i}{\tau_k} = \frac{\tau_i}{\sqrt{\nu/\epsilon}} \tag{2.18}$$

The Stokes number is defined as the ratio of particle relaxation time (τ_i) to the Kolmogorov timescale (τ_k). If: St ≤ 1, particles will follow the fluid streamlines; and if St > 1, particles will be relatively unaffected by fluid motion. Camp and Stein (1943) later suggested substitution of the velocity gradient (*du / dy)* with the mean shear rate given by the inverse of the Kolmogorov timescale. This equation is again only valid for the viscous sub-range of turbulence, as indicated in Equation 2.19:

$$Z_{shear} = \frac{4}{3}(d_i + d_j)^3 \left(\frac{\epsilon}{\nu}\right)^{1/2} \tag{2.19}$$

Saffman and Turner (1956) also developed an equation for turbulent conditions that stemmed from the Von Smoluchowski equation. The equation was found to be similar to the expression developed by Camp and Stein (1943) but differed in the constant. In order for the Saffman and Turner (1956) equation to apply, $(r_i + r_j)^3$ must be smaller than the smallest eddies and the particles must follow fluid motion without deviation, as indicated in Equation 2.20:

$$Z_{shear} = \sqrt{\frac{8\pi}{15}}(d_i + d_j)^3 \left(\frac{\epsilon}{\nu}\right)^{1/2} \tag{2.20}$$

2.4.1.1.3 Accelerative method

The accelerative mechanism applies to collisions that occur in a low turbulence environment by accounting for the inertial effect of particles and bubbles. Collisions between particles and bubbles occur within a shear flow field, but they deviate from fluid streamlines due to particle inertia (see Table 2.1). Saffman and Turner (1956) developed an equation for this mechanism by

adding an inertial term to Equation 2.20 to account for the spatial variations of turbulent motion between particles and the fluid, as indicated in Equation 2.21:

$$Z_{acc} = \left(\frac{8\pi}{3}\right)^{1/2} (r_i + r_j)^2 \left[3\left(1 - \frac{\rho_p}{\rho_f}\right)^2 (\tau_i + \tau_j)^2 \overline{\left(\frac{du}{dt}\right)^2} + \frac{1}{3}(r_i + r_j)^2 \frac{\epsilon}{\nu}\right]^{1/2} \quad (2.21)$$

where $\overline{\left(du/dt\right)^2}$ is the average acceleration of eddies in the viscous dissipation sub-range given by:

$$\overline{\left(\frac{du}{dt}\right)^2} = 1.2\left(\frac{\epsilon^3}{\nu}\right)^{1/2} \quad (2.22)$$

Williams and Crane (1983) also developed an equation for this mechanism based on a turbulent spectrum (Equation 2.23):

$$Z_{acc} = \sqrt{\frac{8\pi}{3}}(r_i + r_j)^2 \sqrt{3w_{accel}^2} \quad (2.23)$$

The model includes an added mass term (w) for particle motion in a liquid environment, but it lacks the turbulent shear mechanism component, rendering it incomplete.

2.4.1.1.4 Purely accelerative mechanism

This is the mechanism that applies in cases where there are high turbulent flows or when large particles are encountered. Particles and bubbles are thrown randomly from eddy to eddy and collisions occur because of relative motion (see Table 2.1). Under these conditions, the viscous eddies become too small to contain particles and bubbles. Abrahamson (1975) developed a collision rate expression for the above conditions, as indicated in Equation 2.24 below, given the particle and bubble velocity distributions:

$$Z = \sqrt{8\pi}\left(r_i + r_j\right)^2 \sqrt{\left(u_i^2 + u_j^2\right)} \tag{2.24}$$

The validity of the above equation is based on independence of the particle and bubble velocities. The Abrahamson model has been used extensively to predict collision rates in turbulent systems (Schubert, 1999; Bloom and Heindel, 2002; Pyke *et al.*, 2003; Sherrel, 2004; Ralston *et al* 2005) despite the model being more suited to particle-particle collisions.

Bloom and Heindel (2002) argued that the inclusion of particle settling velocities (v_{ps}) and bubble rise velocities (v_b) to the Abrahamson model would make it more applicable to most flotation conditions (see Equation 2.25).

$$Z = \sqrt{8\pi}\left(r_i + r_j\right)^2 \sqrt{\left(u_i^2 + u_j^2\right)} \exp\left(\frac{\left(\left|v_{ps}\right| + v_b\right)^2}{2\left(u_i^2 + u_j^2\right)}\right) \tag{2.25}$$

However, the Abrahamson model is often used. Its applicability to different situations is often dependent on the velocity correlations used to determine particle and bubble fluctuating velocities.

2.4.1.1.5 Intermediate correlations

The previous two approaches (shear and accelerative mechanisms) only apply to either the viscous or inertial sub-range of turbulence. Currently, the Saffman and Turner model and the Abrahamson model are the two major models that exist for particle-bubble collisions under turbulence: the former being for the shear mechanism and the latter for the accelerative mechanism. Several authors (Williams and Crane, 1983; Yuu, 1984; Kruis and Kusters, 1997) have attempted to bridge these two approaches by finding more concise models that can predict collisions in both regimes.

Yuu (1984) derived a model that accounts for both shear and accelerative mechanisms for particles smaller than the Kolmogorov microscale, assuming that gravity and Brownian motion have no effect on the collision rate. More recently, Kruis and Kusters (1997) integrated the approach of Williams and Crane (1983) and Yuu (1984) by including an added mass term for

particle motion in a liquid environment. The Kruis and Kusters model is similar to the Abrahamson model but differs in the calculation of the fluctuating velocity:

$$\beta_{\text{Kruis+Kusters}} = \sqrt{\frac{8\pi}{3}}\left(r_i + r_j\right)^2 \sqrt{\left(w_{\text{shear}}^2 + w_{\text{accel}}^2\right)} \tag{2.26}$$

$$\frac{w_{\text{shear}}^2}{v_f^2} = 0.238b\left(\frac{v_i^2}{v_f^2}\frac{\theta_i}{C_{c,i}} + \frac{v_j^2}{v_f^2}\frac{\theta_j}{C_{c,j}} + \sqrt{\frac{\theta_i\theta_j}{C_{c,i}C_{c,j}}\frac{v_i^2 v_j^2}{v_f^2}}\right) \tag{2.27}$$

$$\frac{w_{\text{accel}}^2}{v_f^2} = 3(1-b)^2\frac{\gamma}{\gamma-1}\left[\left(\theta_i+\theta_j\right) - \frac{4\theta_i\theta_j\sqrt{\frac{1+\theta_i+\theta_j}{(1+\theta_i)(1+\theta_j)}}}{\left(\theta_i+\theta_j\right)}\right]\left(\frac{1}{(1+\theta_i)(1+\theta_j)} - \frac{1}{(1+\gamma\theta_i)(1+\gamma\theta_j)}\right) \tag{2.28}$$

where b is the added mass coefficient given by:

$$b = \frac{3\rho_f}{2\rho_i + \rho_f} \tag{2.29}$$

γ is the turbulence constant:

$$\gamma = \frac{2T_L^2}{(15\,\nu/\epsilon)^4} \tag{2.30}$$

and θ_i is the dimensionless relaxation time:

$$\theta_i = \frac{\tau_i}{T_L} \tag{2.31}$$

The above model is able to predict the collision rates of a combination of the shear and accelerative mechanism. Work done by Sherrel (2004) showed that the incorporated mass effects obtained collision rates higher than that of Saffman and Turner (1956), which reduce to the Abrahamson model at higher particle Stokes numbers. However, the major weakness of the Kruis and Kusters model is that it has only been derived for particle-particle interaction and is

not applicable to heterogeneous collisions. The model only allows one particle density input in the added mass coefficient and thus cannot be applied to flotation systems because of the vast difference in particle and bubble densities.

2.4.1.1.6 Velocity correlations for collision frequency

Velocity correlations for particle motion in turbulent media are often derived from the Tchen equation. Levins and Glastonbury (1972) were the first to derive an equation for particle motion in turbulent media by analyzing particles oscillating in a fluid. Assuming single frequency oscillation, they solved the Tchen equation for a particle accelerating relative to the surrounding fluid:

$$\frac{\overline{u_p^2}}{\overline{u_f^2}} = \frac{aT_L + b^2}{aT_L + 1} \tag{2.32}$$

where

$$a = \frac{36\mu}{(2\rho_i + \rho_f)d_p^2} \tag{2.33}$$

and

$$b = \frac{3\rho_f}{(2\rho_i + \rho_f)} \tag{2.34}$$

and T_L is the Langragian integral time scale

$$T_L = \frac{0.7\bar{u}_f^2}{\epsilon} \tag{2.35}$$

Abrahamson (1975) went on to simplify the Levins and Glastonbury equation (Equation 2.26) by assuming that $b \approx 0$ for solid particles in a gas and $a = 1 / \tau_p$ because the density of the fluid is much smaller that the density of the particles. This leads to the following equation:

$$\frac{\bar{u}_p^2}{\bar{u}_f^2} = \left(1 + 1.5\frac{\tau_i \epsilon}{u_f^2}\right)^{-1} \tag{2.36}$$

However, the above equation is only valid for inertial sub-range eddies (St ≤ 1). Liepe and Moeckel (1976) developed a model from experimental work for the root mean fluctuating velocity at intermediate values of the Stokes number. This model has been used in many publications together with the Abrahamson collision frequency equation and is thought to be more appropriate for a flotation system:

$$u_i = 0.4\frac{\epsilon^{4/9} d_i^{7/9}}{\nu^{1/3}}\left(\frac{\rho_i + \rho_f}{\rho_f}\right)^{2/3} \tag{2.37}$$

Brady *et al.* (2006) validated this model experimentally using a small-scale water tunnel that generated homogeneous isotropic turbulence (See Figure 2.5). Turbulence in this system is generated by a grid of circular cylinders 1 cm in diameter spaced at 1 cm in both length and width directions. Isotropic turbulence was created in this model flotation cell through grid turbulence. The results from this work showed that the Liepe and Mockel model (Equation 2.31) closely predicts the fluctuating velocity of 80 µm particles with a 12% error.

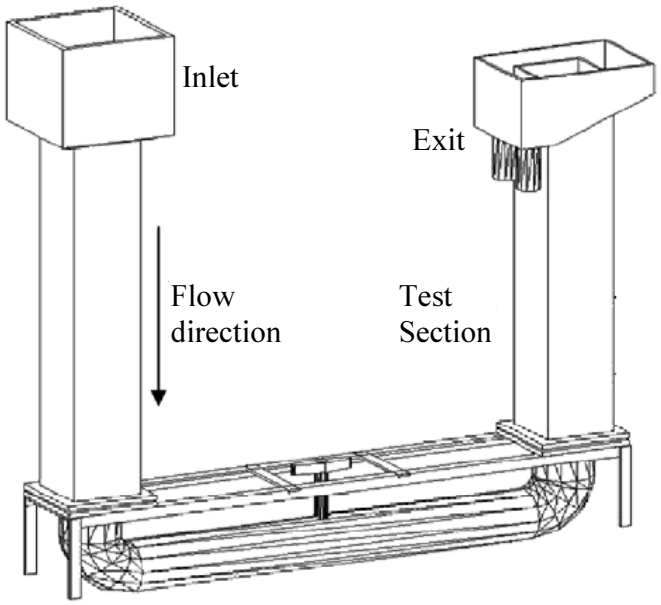

Figure 2.5. Schematic of water tunnel used for flotation tests by Brady *et al*. (2006).

However Brady *et al.* (2006) found that the Levins and Glastonbury model (Equation 2.32) and the Abrahamson model (Equation 2.24) were in agreement with the bubble RMS velocities, but both did not do as well in predicting particle RMS velocities. An alternative equation was derived for the bubble fluctuating velocity by Lee and Erickson (1987);

$$\overline{u_b^2} = 2(\epsilon d_b)^{2/3} \tag{2.38}$$

This model has been used in some modelling applications (Sherrel, 2004), despite being proved to over-predict bubble fluctuating velocities (Brady *et al.*, 2006).

2.4.2 Experimental findings

Over the past few decades there have been numerous studies done in which flotation rates/recoveries were investigated as a function of agitation, particle size, particle density and bubble size. Practically all of these studies demonstrated that increasing agitation improves the rate of flotation of fine particles (Mackenzie and Matheson, 1963; Sun and Zimmerman, 1950; Kirchberg and Topfer, 1965; Schubert and Bischofberger, 1978; Malhotra *et al.*, 1980; Varbanov, 1984; Ahmed and Jameson, 1985; Jordan and Spears, 1990; Deglon, 2002; Li *et al.*, 1990; Pyke *et al.*, 2003; Newell and Grano, 2006). The majority of these studies were on normal flotation bubbles and the few studies on micro bubbles found that far lower levels of agitation are required for optimum flotation (Ahmed and Jameson, 1985; Deglon, 2002).

Some studies have attempted to quantify the increase in the rate of flotation with increasing agitation. Nonaka *et al. (*1982), Saint Amand (1999) and Deglon (2002) found that the rate of flotation increases with the specific power input to the power of 0.75, 0.50 and 0.91 respectively, while Newell and Grano (2006) found that this is approximately proportional to the level of agitation.

Deglon (2002) determined an empirical correlation for the attachment rate constant as a function of specific power input, particle size and bubble size. The equation was found to be applicable to fine particles (3 - 30 μm) and a bubble size range of 0.1 – 0.8 mm. However, because this attachment rate constant accounts for both collision and attachment effects, the power of 0.91 for

the specific power input is higher than that found by Nonaka *et al.* (1982) and Saint Amand (1999).

Newell and Grano (2006) performed flotation tests on methylated quartz with a d_{50} of 40 µm in a 2.25 dm^3 laboratory scale Rushton turbine flotation cell similar to those used by Ahmed and Jameson (1985), Deglon (2002), Pyke *et al.* (2003) and Sherrel (2004). They found that the undistributed rate constant is approximately proportional to the level of agitation for energy dissipation rates up to 4.1 W/kg; yet increasing the energy dissipation from 4.1 W/kg to 12.6 W/kg had very little effect on the overall rate constant.

2.5 Grid agitation

Oscillating grids originated from the classical experimental studies on 'grid turbulence', in which regions of near homogeneous, isotropic turbulence were obtained by passing fluid through a stationary grid (Mohamed and LaRue, 1990) or dropping a grid through a stationary fluid (Dickey and Mellor, 1980). However, due to the rapid decay of turbulence downstream from the grid, these configurations proved impractical for many experimental studies (Srdic *et al.*, 1996). As a consequence, oscillating grid systems were developed, whereby a grid was continually moved back and forth through the fluid, resulting in a more practical 'static turbulent region' for conducting experiments. Numerous studies on oscillating grids have shown that regions of near homogeneous, isotropic turbulence can be attained in vessels using this form of agitation (Thompson and Turner, 1975; Hopfinger and Toly, 1976; Tsai and Lick, 1986; DeSilva and Fernando, 1992; Shy *et al.*, 1997; Eidelman *et al.*, 2006).

2.5.1 Single-grid systems

Typically, the apparatus used for these tests includes: a transparent tank, which may be rectangular or cylindrical; a grid that is either horizontally or vertical oriented; and an oscillating drive device. The grid is made in a square array, with the mesh size, *M,* oscillates around its mean position by an amplitude/stroke *S* at a frequency *f*. In order to generate homogeneous and isotropic turbulence, the grid solidity should be less than 40% (Hopfinger and Toly, 1976). This is because the final turbulence is a result of wake interaction from pockets of turbulence formed

on either side of the bars of the grid. Grid solidities greater than 40% have turbulence that originates from jets that come about because the velocity of fluid in the holes exceeds the velocity of the grid.

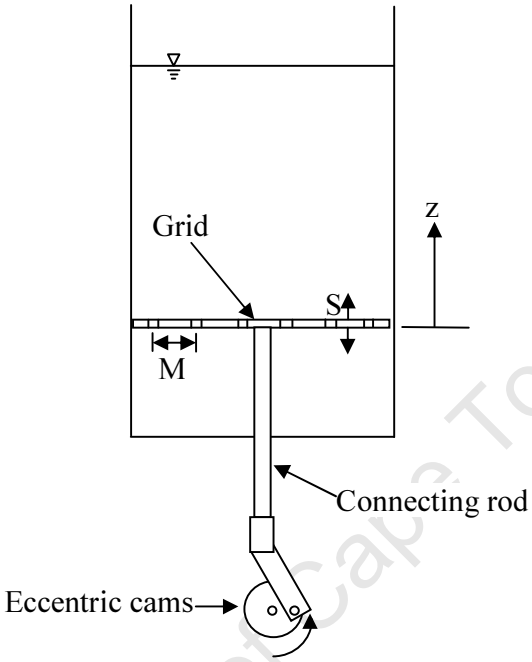

Figure 2.6. Schematic of a typical single grid mixer

Studies of turbulence generated by one oscillating grid in a water tank facilitated estimation of the decay law of turbulence and the dependence of turbulence parameters on the mesh size, frequency and amplitude of grid oscillations. Using a vertically oscillating one-grid configuration in a water tank, Thompson and Turner (1975) found that RMS fluctuating velocity was linearly dependent on frequency (*f*) and inversely proportional to distance from the mid-plane of the oscillating grid, *z*, to the power 1.5. A year later, Hopfinger and Toly (1976) developed the decay law for turbulence in an oscillating grid system. The equations (Equation 2.39 and 2.40) are given by the RMS fluctuating velocity:

$$u_x = u_y = \frac{C_1 M^{0.5} S^{1.5} f}{z} \tag{2.39}$$

$$u_z = \frac{C_2 M^{0.5} S^{1.5} f}{z} \tag{2.40}$$

$$l = c_l z \tag{2.41}$$

C_1 and C_2 are tank-geometry dependent constants, which were found to be 0.25 and 0.27 respectively (Hopfinger and Toly, 1976). The turbulent integral scale, l, was found to be proportional to distance from the grid, where $c_l \approx 0.12$. Substituting the physical parameters *M, S, f* and *z* in the definition of TKE given by Equation 2.13, the turbulent energy in an oscillating grid cell can be estimated as:

$$\mathrm{TKE(k)} = \frac{1}{2}(2C_1^2 + C_2^2)\left(\frac{M^{0.5} S^{1.5} f}{z}\right)^2 = \alpha \frac{M S^3 f^2}{z^2} \tag{2.42}$$

Orlins and Gulliver (2003) used a two-component LDV system and Ura *et al.* (1987) and DeSilva and Fernando (1992) used a standard LDV to confirm that the expressions developed were correct. The authors, however, found different constants, depending on grid configuration:

Table 2.2. Table showing the different values for constants C_1 and C_2

Authors	**Measurement technique**	S/M	S/d	**C_1**	**C_2**
Hopfinger and Toly (1976)	Hot-film probe	1	5	0.25	0.27
Ura *et al.* (1987)	Hot-film probe	0.2, 0.8 and 0.13	1.0, 0.25 and 0.13	0.20	0.19
DeSilva and Fernando (1992)	Standard LDV	0.26 and 0.18	1.30 and 0.94	0.22	0.26
Kit *et al.* (1997)	Hot-film probe	0.40	1.66	0.50	0.55
Eidelman *et al.* (2002)	DPIV			< 0.25	< 0.27
Orlins and Gulliver (2003)	2-component LDV	0.48	2.36	0.22	0.26

Kit *et al.* (1997) proposed that the values of the constants C_1 and C_2 vary with the geometric parameters of the grid if $S / M \leq 0.4$ and $S / d \geq 4$. However, the data given in Table 2.2 show no clear trend. The z component value of the RMS velocity (C_2) is always greater that the value of the x and y components of the RMS velocity (C_1) because of the uni-directional motion of the grid. However the anisotropy due to this effect, C_2 / C_1, rarely exceeds 1.1.

Orlins and Gulliver (2003) performed a study in which they designed an oscillating grid chamber and performed tests to quantify the shear-free turbulence produced in water. Figure 2.7 shows that for the given conditions, decay laws are consistent with the data. However, it should be noted that as distance from the grid increases, the data closely approaches the empirical decay laws. Reynolds stress, as calculated from LDV measured velocities, has an average of zero. The absolute values of the individual measurements are very small ($\leq 2 \times 10^{-4}$ m^2s^{-2}), mainly because the mixing system employed here has no overall shear.

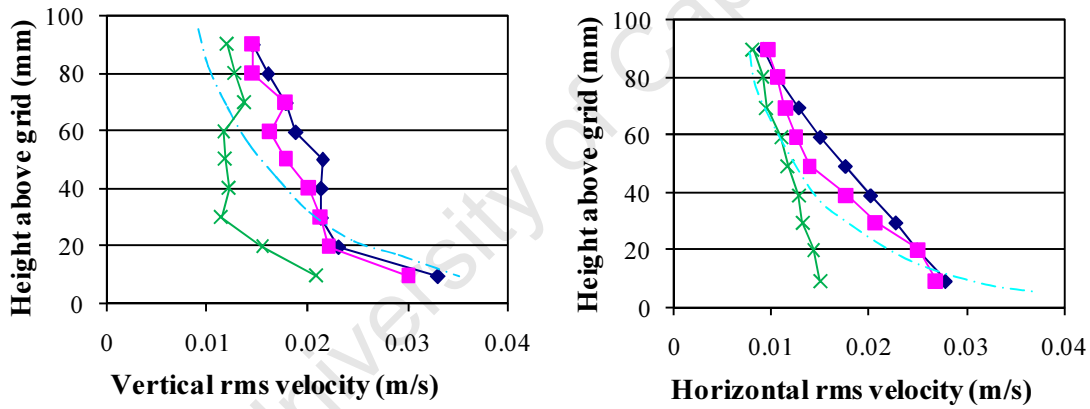

Figure 2.7. RMS velocity profiles in an oscillating grid cell. Data obtained from Orlins and Gulliver (2003).

The power spectra can be used to determine the rate of energy dissipation around an oscillating grid using Tennekes's (1975) definition for the Eulerian spectrum for isotropic turbulence without mean flow. The definition is given by equation 2.43, where ϕ is the kinetic energy per unit frequency, f, $q^2/2$ is the mean kinetic energy per unit mass, and α is an unknown constant.

$$\phi(f) = \frac{\alpha \epsilon^{2/3} q^{2/3}}{f^{5/3}} \tag{2.43}$$

$$\bar{\epsilon} = \frac{1}{h} \int_{-h/2}^{h/2} \epsilon \, dz \tag{2.44}$$

Bache and Rasool (1996) developed an approach in which they matched energy losses from the stirred tank to the power input into the system to obtain α and therefore ε via Equation 2.44. The average rate of energy dissipation, $\bar{\epsilon}$, is determined by grid power input measurements found by directly measuring the power added to the system by a force transducer and subtracting all the known losses (such as skin friction along the shaft and energy losses associated with bearings). The integral on the right-hand side, which contains α, is determined from the power spectra measurements using LDA. The grid power input was correlated with the frequency and amplitude parameters as a scale of the velocity input. The corresponding power *P* for a grid with plan area *A* and solidity σ is expressed by

$$P = \frac{C_p \rho \nu^{1/2} (fS)^{5/2} \sigma A}{d^{1/2}} = m_L \bar{\epsilon} \tag{2.45}$$

Spectral analysis indicated that above the grid, the RMS velocity components (u_x, u_y and u_z) values below the grid were fairly similar to each other. This is indicative of a state of isotropy. Above the grid, however, u_x and u_y were identical but this was due to persistence of the vertical component, u_z / u_x = 1.2. A generalized distribution function was fitted to the power spectra, given by Equation 2.46. This function was found to describe well the spectra trends above, below and within the grid at different driving frequencies.

$$E(f) = \frac{A}{B^{5/3}} \frac{u^2 f_{max}^{2/3}}{f^{-5/3}} \tag{2.46}$$

By assuming that Equations 2.43 and 2.46 are equal, an equation for ϵ can be obtained. With knowledge of $\bar{\epsilon}$ from Equation 2.45, an energy balance (Equation 2.44) can be applied to obtain the value of α and hence an empirical relationship for ϵ.

$$\epsilon = \gamma u^2 f_{max} \tag{2.47}$$

where

$$\gamma = \frac{(2\pi)^{5/2} A^{2/3}}{\alpha^{3/2} B^{5/2}} \tag{2.48}$$

Over a range of driving frequencies, the combined representative value for α over the three component directions was 1.87 ± 0.46 (SD), with the parameter γ = 11.3 ± 1.2 (SD). The values A and B are spectra fitting parameters. An important observation was that the coefficient γ was independent of distance from the grid. The authors went on to introduce the Eulerian integral time scale τ_E of turbulence as a principal scaling factor, which is defined via the auto-correlation function R(t)

$$R(t) = \frac{\int_0^\infty E(f) \cos(2\pi f t)\ df}{\int_0^\infty E(f)\ df} \tag{2.49}$$

and $$\tau_E = \int_0^\infty R(t) dt \tag{2.50}$$

They observed that, for the entire data set, the non-dimensional integral time scale $\tau_E f_{max}$ was constant at 0.21. This allowed Equation 2.47 to be rewritten in the form of Equation 2.51, which is a more convenient route for determining ϵ in the frequency domain of energy-containing eddies.

$$\epsilon = \gamma_1 \frac{u^2}{\tau_E} \tag{2.51}$$

where γ_1 is = 2.4 ± 0.5 (SD), as estimated on the basis of Equations (2.44), (2.45) and (2.51) i.e.

$$\gamma_1 = \frac{h\bar{P}_g/m_L}{\int_{-h/2}^{h/2} u^2/\tau_E \, dz} \tag{2.52}$$

Schulz and Chaudhry (1998) and Matsunaga *et al.* (1999) obtained theoretical predictions of the turbulent kinetic energy, k, and its dissipation rates, ε, for oscillating grid turbulence using the k–ε turbulence model. Assuming that there is no mean flow and that the only statistical quantity variations occur in a vertical direction, the k-ε model is given as

$$\frac{\nu_t}{\sigma_k}\frac{\delta}{\delta x}\left(\frac{\delta k}{\delta x}\right) = \varepsilon \tag{2.53}$$

$$\frac{\delta}{\delta z}\left(\frac{\nu_t}{\sigma_k}\frac{\delta \varepsilon}{\delta z}\right) = C_2\frac{\varepsilon^2}{k} \tag{2.54}$$

$$\nu_t = C_\mu\frac{k^2}{\varepsilon} \tag{2.55}$$

with the following boundary conditions:

$k = k_0, \varepsilon = \varepsilon_0 \text{ at } z = 0$

$k \to 0, \varepsilon \to 0 \text{ as } z \to \infty$

where ν_t is the eddy viscosity and σ_k, σ_ε, C_2 and C_μ are constants for the model.

After solving equations 2.53 and 2.54 with the boundary conditions given using dimensional analysis, the following analytical solutions are obtained:

$$\frac{k}{k_0} = \left(\frac{z}{1.82}\left(\frac{\varepsilon_0^2}{k_0^3}\right)^{1/2} + 1\right)^{-5} \tag{2.56}$$

$$\frac{\varepsilon}{\varepsilon_0} = \left(\frac{z}{1.82} \left(\frac{\varepsilon_0^2}{k_0^3} \right)^{1/2} + 1 \right)^{-8.5} \tag{2.57}$$

$$l_t = \left(\frac{z}{1.82} \left(\frac{\varepsilon_0^2}{k_0^3} \right)^{1/2} + 1 \right) \tag{2.58}$$

where l_t is the characteristic length scale; k_0 and ε_0 are constants linearly dependent on $(S/M)^{1/4}$ and (S/M) respectively.

When

$$\frac{z}{1.82} \left(\frac{\varepsilon_0^2}{k_0^3} \right)^{1/2} \gg 1 \tag{2.59}$$

there is, however, a significant difference in the decay laws predicted analytically by the k–ε model and those obtained empirically by other researchers. The exponent of the decay laws predicted by the k – ε model for the TKE, k, and the dissipation rate are -5, and -8.5 respectively whereas the empirical exponents suggested by several authors (Hopfinger and Toly, 1976; DeSilva and Fernando, 1992) from their experiments were -2, and -4. Matsunaga *et al.* (1999) showed that the k–ε model was valid on the basis of their experimental data. Janzel *et al.* (2003) compared experimentally obtained vertical profiles of turbulent kinetic energy with theoretical predictions of the k–ε turbulence model and concluded that the profiles generated by the analytical solution agree with those of the experimental turbulence kinetic energy data.

The use of a k–ε model to describe turbulence created by oscillating grids is questionable. The turbulence created by oscillating grids has a zero mean shear, but this model is built in the framework of turbulence with a mean shear and the constants of the steady k–ε model were determined from experiments with mean shear flows.

It should be noted, however, that the empirical relationships developed thus far do not hold until one reaches a substantial distance from the grid. However, several relationships have been proposed in literature for the limiting distance beyond which the decay laws are applicable. DeSilva and Fernando (1992) found that the decay laws held for $z \geq 4S$. Atkinson *et al*. (1987) recommended a reading be taken in the region of $3M \geq z \geq 2M$ for approximately homogeneous turbulence. In this region, turbulence is highly non-linear, even at low $R_{lo,}$ because TKE transport in this region can only take place via the non-linear energy flux-divergence term of the TKE equation (Orlins and Gulliver, 2003). A limiting oscillation frequency of 7 Hz, above which the u_{rms} is no longer linearly related to *f,* was pointed out by McDougall (1979).

2.5.2 Two grid systems

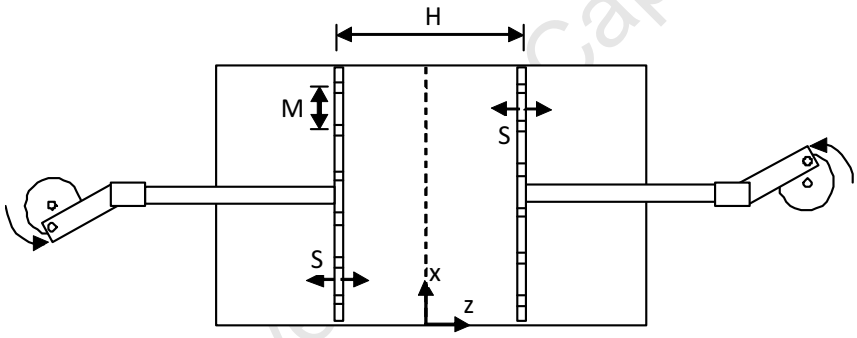

Figure 2.8. Schematic of a typical two-grid system

Single-grid systems tend to produce bias in the RMS turbulent velocity in the direction of oscillation. To compensate for this, a two-grid configuration (c.f. Figure 2.8) became a popular choice amongst researchers (Srdic *et al.*, 1996; Shy *et al.*, 1997; Eidelman *et al.*, 2006). The spatial decaying turbulence of both grids interacts to form a substantial nearly isotropic stationary region in between the grids, which is often the domain of interest. Villermaux *et al.* (1995) proposed that the power released into the system by each grid was directly additive, assuming that the integral length near the central region between the two grids was equal to that given by one grid:

$$u_{eff} = 2^{1/3} u_{rms} \tag{2.60}$$

where u_{rms} is the RMS velocity as given by Equation 2.39 for one of the grids.

The velocity measurements from work by Shy *et al.* (1997) confirmed energy released per unit time by each grid is directly additive in support of the above prediction.

Shy *et al.* (1997) further developed an expression for their 2-grid system, which did not vary very much from the Hopfinger and Toly expression (Equation 2.39). The equation is:

$$u = \frac{0.89 M^{0.5} S^{1.5} f}{H^{1.5}} \tag{2.61}$$

The expression gives a good estimate of turbulence intensity for the range $4 \leq H/M \leq 6$, where H is the distance between the two grids. This region has been shown to produce some properties of isotropic stationary turbulence with variations between horizontal and vertical RMS velocity values of less than 15% (Shy *et al.*, 1997). The flow condition to which the equation best applies is frequencies between 1 and 8 Hz and a ratio $S/M = 2/3$.

The turbulence integral scale below was estimated by Eidelman *et al.* (2002) based on data developed by Hopfinger and Toly (1976) with the distance, z, in a range $S/M = 0.2 - 0.9$.

$$l = \frac{S}{M} c_0 z \tag{2.62}$$

Two distinct flow regions are developed: the first is a high turbulent flow region near the grid; the second is a nearly isotropic turbulent flow region away from the grid. Srdic *et al.* (1996) found that in the highly turbulent region near the grids ($1 \leq z/M \leq 2$), turbulence intensity was inversely proportional to distance from the grid at the centre of the grid mesh and inversely proportional to the distance from the grid to the power 2. The difference vanishes at $z/M \geq 2$ with the inverse proportionality power coming to 1.1.

2.5.3 Multi-grid systems

Several studies have used stacks of oscillating grids, discs and plates as a substitute for impellers for mixing in reactors. This type of agitation is used in reactors that require knowledge of local rates of energy dissipation, such as coagulation kinetics studies (Brunk *et al.*, 1998). Multi-grid agitators are particularly good for studying transport phenomena because of the uniformity of turbulence and energy dissipation they display. The following section gives the turbulent characteristics in an oscillating multi-grid mixer. This is a review of the work done by Bache and Rasool (2001). The equipment described here was used as the test apparatus for the study done by this author.

2.5.3.1 Description of the multi-grid mixer

The mixer used by Bache and Rasool (2001) is shown in Figure 2.9 below. The multi-grid mixer consists of 19 grids stacked on a drive shaft with equal spacing of 18 mm. The grids are made of 1 mm woven wire mesh with 8 X 8 mm square grid holes. The drive shaft is connected to a sinusoidal crank assembly with a motor and gearbox that has a frequency of 0.1 – 3.1 Hz. A Kistler forcer transducer was placed on the drive shaft to measure instantaneous forces translated into average power. Turbulence measurements were done by LDA using an externally mounted probe.

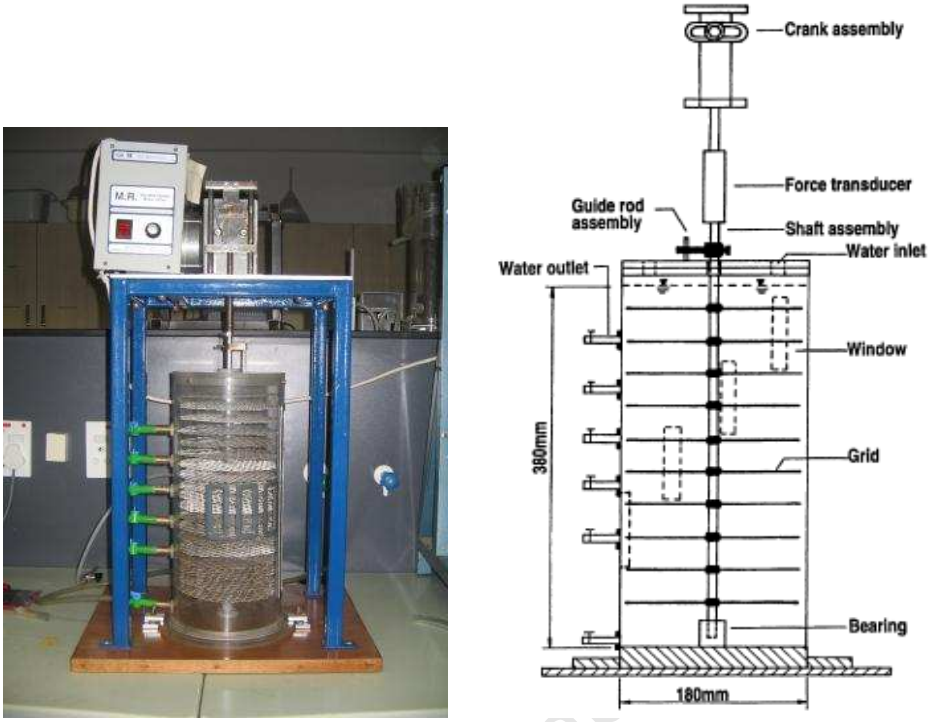

Figure 2.9: Pictorial and schematic diagram of the multi-grid mixer (Bache and Rasool, 2001)

2.5.3.2 Turbulence characteristics

Turbulence measurements were made using a one component dual beam system LDA that measured the horizontal (*u*) and vertical (*v*) rms velocity. The time integral scale for each component was determined from the spectral analysis. In order to cater for anisotropy (particularly in the region swept by the grids, where $w^2 \approx 4u^2$) a representative timescale, τ_E, and an average intensity per component, U^2, are defined as follows:

$$U^2 = \frac{1}{3}(2u^2 + w^2) \tag{2.63}$$

$$\tau_E = \frac{(2u^2\tau_u + w^2\tau_w)}{3U^2} \tag{2.64}$$

The horizontal turbulence components are assumed to be identical.

Figure 2.10 shows the spatial variation of energy, U^2, timescale, τ_E, and energy dissipation, U^2/τ_E for the set of 19 grids. Every fluid element within the sample volume is swept by the grid and the turbulence parameters are reasonably uniform with typical scatter. The turbulence field created by individual grids merge, though evidence of the character of individual grid turbulence exists. The figures show that U^2 and U^2/τ_E is at its minimum at the extremes of the stroke and at a maximum at the centre. This is because U^2 is driven by the grid's instantaneous velocities. On the other hand, the timescale τ_E is nearly constant, because it is largely a function of the frequency.

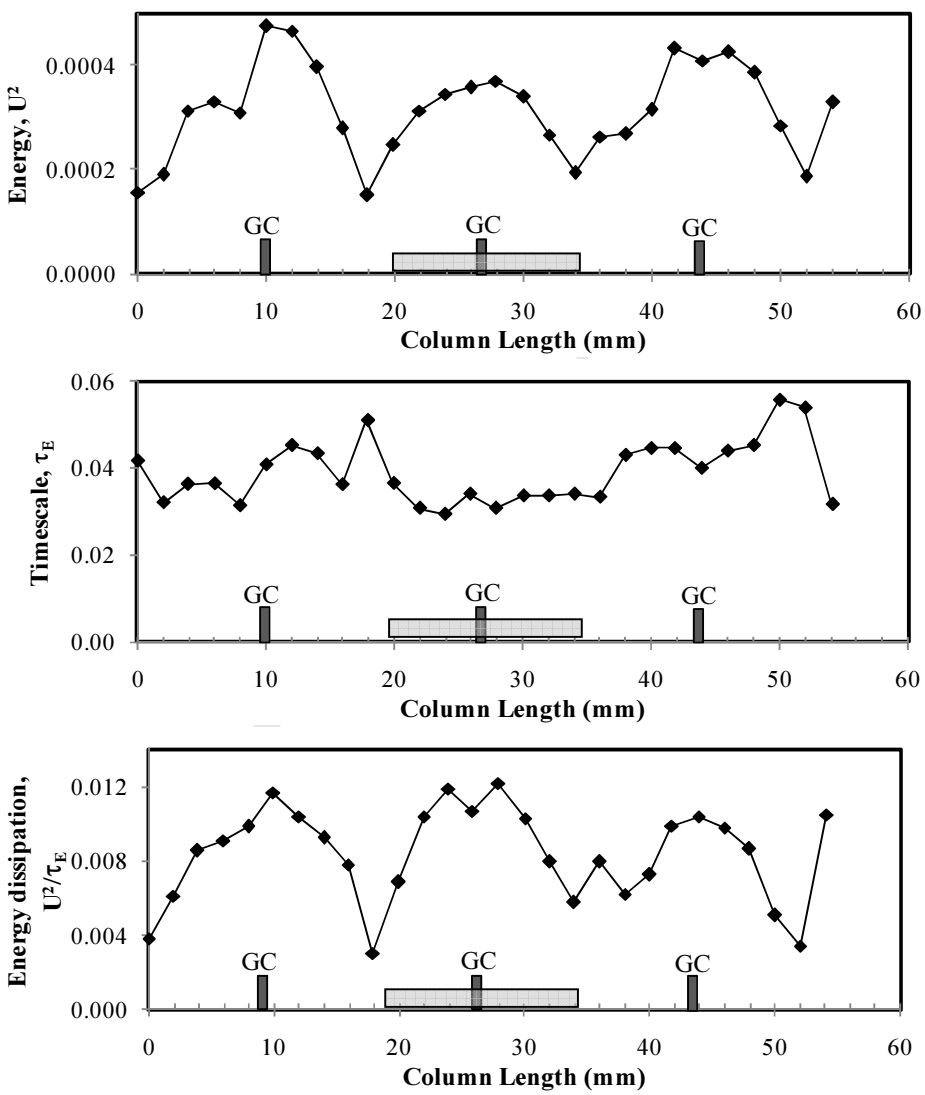

Figure 2.10: Plot showing 19 grid data at f = 2.05 Hz, S = 18.17 mm, L = 17 mm.

2.5.3.3 Power characterisation

The Kistler force transducer was used, to determine the average power input per grid. Based on the data collated by Bache and Rasool (1996), power input per grid, P_1, was defined by Equation 2.65 as follows:

$$P_1 = C_p \rho A_c \sigma f^3 S^3 R_N^{-\alpha} \tag{2.65}$$

where $$R_N = \frac{fSd}{\nu} \tag{2.66}$$

C_p is a calibration constant; ρ is the fluid density; A_c is the overall cross section area; σ is the corresponding grid solidarity; and α is the grid Reynolds number, (R_N), coefficient. Equation 2.65 was only regarded as being representative for a similar grid system as used in this particular setup. The equation gives the dependence of the power input on the Reynolds number, R_N. The value of α was found to be 0.35 ± 0.05 (S.D.) using linear regression and C_p was estimated to be 97 ± 22 (S.E.).

The mean energy dissipation rate can be determined by applying the energy balance approach (Bache and Rasool, 1996). Given the energy input per grid, P_1, the mean energy dissipation rate is defined as:

$$\bar{\varepsilon} = \frac{n_g P_1}{m_L} \tag{2.67}$$

where n_g is the number of grids and m_L is the mass of the fluid. This equation forms the basis of all the power input calculations used in this work.

Turbulence parameters (U^2 and τ_E) can also be used to determine the mean energy dissipation rate by making use of Equation 2.45. The average energy dissipation, $\bar{\varepsilon}$, is determined from the measured or calculated power input and the rate of energy dissipation is substituted for Equation 2.52 to obtain the Equation:

$$n_g \gamma \int \frac{U^2}{\tau_E} \, dz = \frac{n_g P_1}{m_L} \tag{2.68}$$

With the aid of numerical integration, the value of the only unknown, γ, can be determined.

2.6 The efficacy of the multi-grid mixer as a flotation research tool

This study investigates the effect of energy input on flotation kinetics of methylated quartz particles in a novel oscillating grid flotation cell. This cell is another form of an agitated column, which uses grids that oscillate vertically to create mixing. The cell decouples the three flotation sub-processes, namely: solids suspension, bubble break up and particle-bubble contacting. This makes optimization of any one of the sub-processes simpler and manageable. The impeller driven flotation cell, on the other hand, has the use of energy coupled into all three sub-processes. To date, all flotation energy studies have been performed in this type of cell.

The multi-grid mixer has more variables, which results in better control of the hydrodynamic environment. The impeller driven cells have one energy control variable: the rotational speed of the impeller.

Above all, oscillating multi-grids generate near ideal hydrodynamic environments over a large region, characterized by turbulence that is relatively homogeneous and isotropic at low energy levels. This makes the device more ideal for investigating the effect of energy/agitation on flotation. Theoretical flotation models are derived from simplified flotation fundamentals – the most common being the use of global variables. To the author's knowledge, this is one of the first studies in which flotation tests have been conducted in a stagnant near ideal turbulent environment.

CHAPTER 3 EXPERIMENTAL

This chapter details the apparatus and experimental procedures used to achieve the objectives outlined in Section 1.4. The chapter gives design details about: the novel oscillating grid cell in Section 3.1, particle preparation in Section 3.2, flotation experimental details in Section 3.3 and hydrodynamic precharacterisation details in Sections 3.4.

3.1 The oscillating grid flotation cell

The oscillating grid flotation cell is based on the oscillatory multi-grid mixer as used by Bache and Rasool (2001). The oscillatory multi-grid mixer was purchased from these authors and retrofitted to produce the oscillating grid flotation cell, as shown in Figure 3.1.

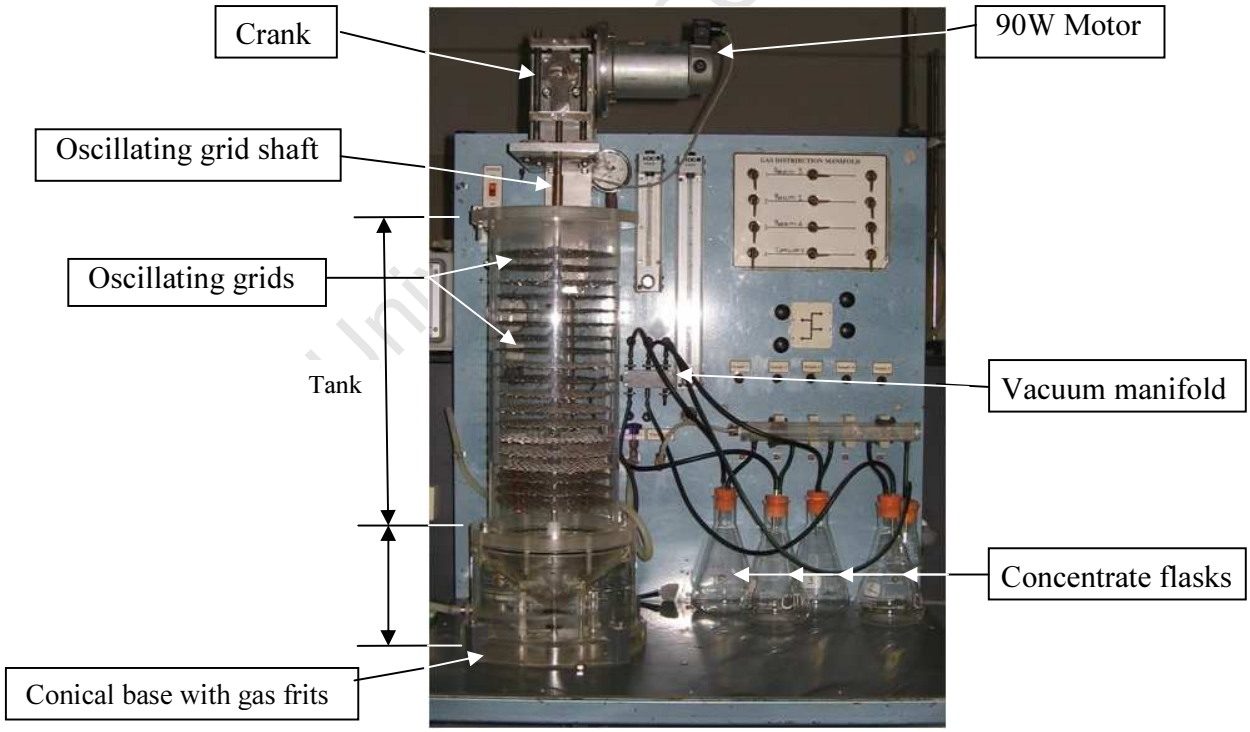

Figure 3.1. The oscillating grid flotation tank.

3.1.1 The flotation tank

The 10-litre flotation tank consists of a cylindrical section and a right-angled conical base held together with flanges. Figure 3.2 shows a schematic diagram of the two sections that make up the flotation tank.

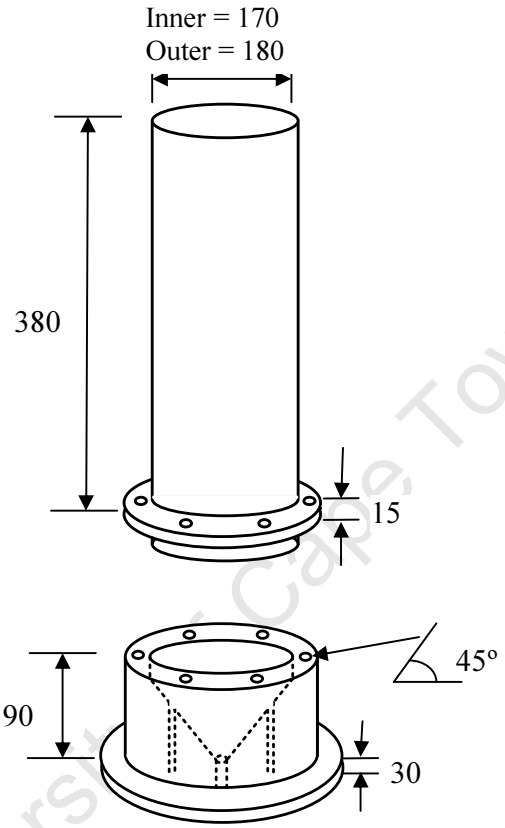

Figure 3.2. Schematic diagram of the flotation tank.

The material chosen for the cylindrical section was 5 mm thick perspex because of its strength, transparency and easiness to clean. This forms the active volume for the flotation process. The conical base was constructed by combining 3 sheets of 30 mm thick perspex, then carefully creating a conical hole in it. This section was bolted down onto the flotation rig stand for stability. The apex of the cone leads to a 10 mm cylindrical discharge hole for the tailings. The base also has four 8 mm vertical holes for the gas frits; these are equidistant from each other such that each hole is at the centre of each quadrant for even gas distribution into the flotation volume.

3.1.2 The grid mixing system

The grid agitation system used in this study is illustrated in Figure 3.3. Grids were formed from 1 mm diameter stainless steel woven wire mesh with a hole size of 8 mm. The drive shaft assembly on which the grids were mounted was supported by PVC collar support at the conical base of the flotation column. The collar support had Teflon bearings to minimize friction. A 90 W motor with a perpendicular shaft gearbox crank assembly provided sinusoidal motion attaining frequencies up to 7.1 Hz.

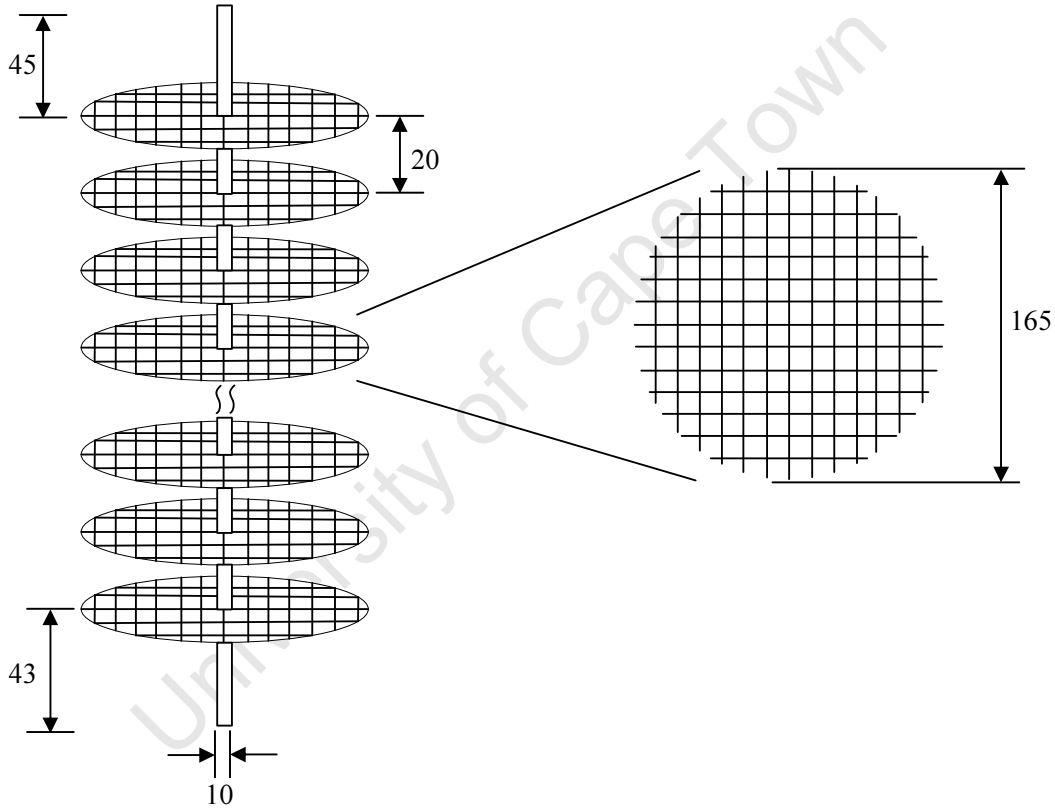

Figure 3.3. Schematic diagram of the grid mixing system.

For purposes of this study, the grids were oscillated at a fixed amplitude, equal to the grid spacing, over the entire range of frequencies, using a variable speed drive. This ensured that the grids swept over the entire test area. The purpose of the oscillating grids in the rig was neither to suspend the solids nor to cause bubble break-up, but to induce a

particular level of turbulence. During the flotation tests, the pulp moved downwards counter-currently to the gas bubbles, making solids suspension unnecessary.

3.1.3 Aeration and froth removal system

The aeration system consists of a nitrogen cylinder from which gas was regulated and fed to the system at a constant pressure of 200 kPa. Nitrogen was chosen as the aeration gas because of its homogeneity (very pure >99.999%) and for consistency with similar flotation energy studies (Ahmed and Jameson, 1985; Deglon, 2002). The nitrogen was passed through a saturator then metered through a 5850S Brooks™ Smart (TMF) mass flow controller before being distributed to a set of four 20 mm sintered glass discs (Glasstech Pty Ltd). A flow diagram of the aeration system is shown in Figure 3.4.

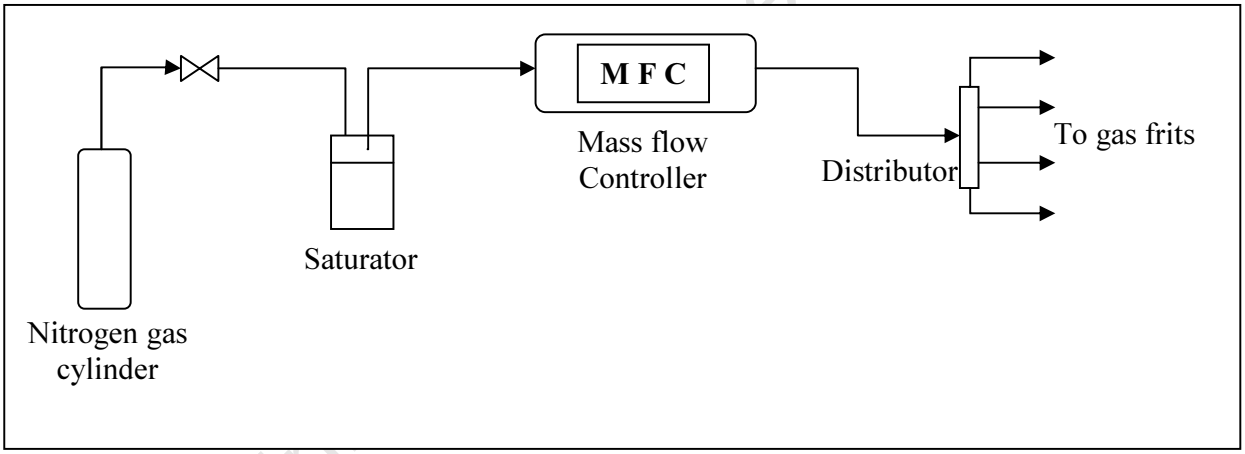

Figure 3.4. Flow diagram of the flotation aeration system.

During the experiments, a suction nozzle connected to a vacuum pump was skimmed over the surface of the liquid to remove the froth that formed. The vacuum pump creates vacuum to a central manifold connected to four 500 ml concentrate flasks which collected the different concentrates at sampling times of 1, 2, 4 and 8 minutes . The vacuum created in the concentrate collection flasks causes suction in the lines connected to the distributor from each of these collection flasks. When a valve is opened, the suction is extended to the distributor and to the

line with the suction nozzle. When the nozzle is skimmed over the liquid surface, froth is drawn up the line, to the appropriate collection flask, determined by the open valve at the distributor.

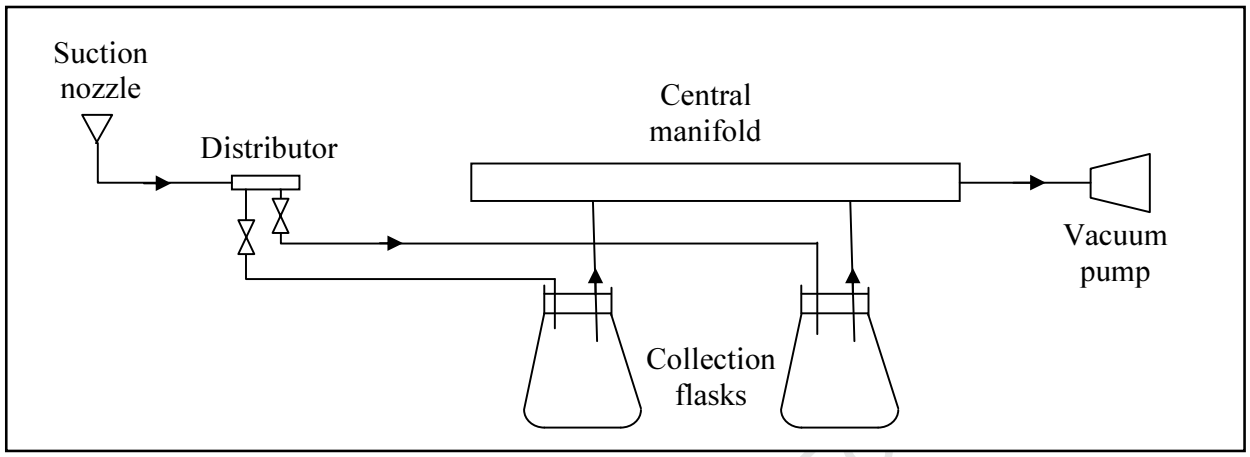

Figure 3.5. Flow diagram of the froth removal system.

3.2 Pre-characterisation experiments

3.2.1 Particle sizing

Three 1 kg high-quality quartz samples (>99.9%) in the size range +1.2 – 2.2 mm were obtained from Sigma-Aldrich™ for this experiment. A milling curve was determined for dry milling the sample in a clean 20 cm diameter ceramic mill with mixed-sized ceramic balls. An appropriate milling time was chosen to suit the generation of -106 µm particles using wet screening. The particles were then sized to give an indication of the feed size distribution for the experiments. Figure 3.6 shows the feed particle size distribution for quartz particles used for this work.

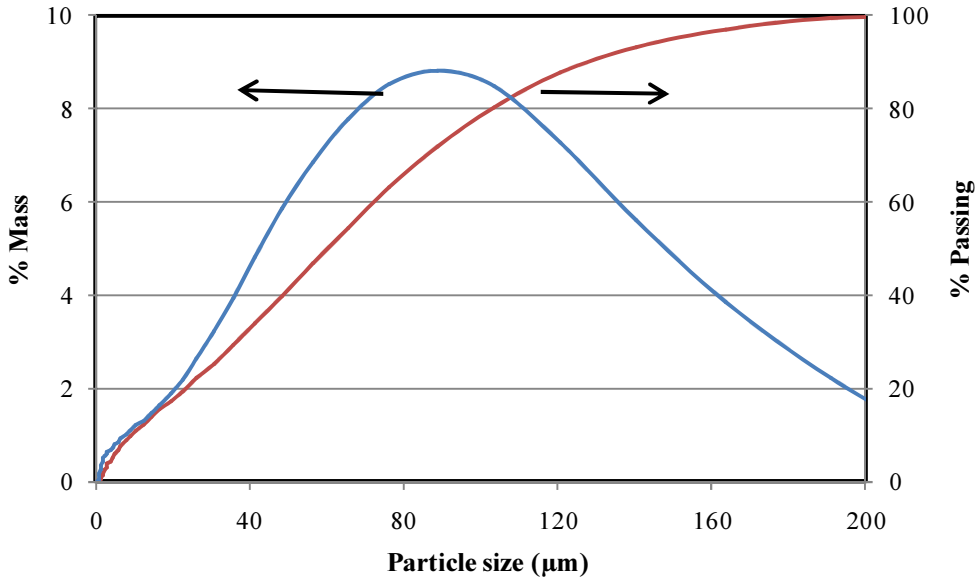

Figure 3.6. Quartz particle size distribution in the flotation feed

Particle size analysis was done using the Malvern Mastersizer™, which is capable of detecting particles as small as 0.06 µm to 800 µm using laser diffraction. The particle size distributions of the flotation concentrates and tailing were determined. Reproducibility of the size measurements was tested by doing two repeat tests on the feed fraction. The results of these tests are presented in Table 3.1 below.

Table 3.1. Particle size analysis of the feed fraction, as given by the Malvern Mastersizer

Particle Size (µm)	% Passing		
	Run 1	Run 2	Run 3
10.5	13.04	12.77	12.54
26.2	26.96	26.13	25.39
48.3	46.93	45.53	43.59
76.3	69.30	68.01	65.78
120.7	90.44	89.91	88.86

The table above shows that the reproducibility of the Malvern Mastersizer™ measurements was very good.

3.2.2 Methylation of quartz

Quartz was methylated to induce hydrophobicity. The methylation procedure was as used originally by Crawford and Ralston, (1988) and subsequently by authors such as Pyke *et al.* (2003) and Newell and Grano (2006), as follows. A 100 g sample of high purity quartz (p_{80} = 100 µm) was placed in a cleaned glass conical flask with a magnetic stirrer bar and heated in an oven overnight. Nitrogen gas was added and the flask was sealed and cooled for 2 hours. 200 ml of 0.01M trimethylchlorosilane (TMCS) in cyclohexane obtained from Sigma-Aldrich™ was added and the mixture was stirred for 10 minutes. The solution was decanted and the quartz rinsed with cyclohexane to remove residual TMCS. The sample was dried overnight in an oven at 110˚C to produce the final hydrophobic quartz. Three kilograms of methylated quartz was generated using this method. This was blended and split into individual feed samples for the flotation tests using a FRITSCH™ rotary sample divider.

3.2.3 Contact angle measurement

The contact angle is commonly determined by sessile drop or sessile bubble techniques. The angle of contact is measured through the vapour or liquid phase of a water drop or bubble on a polished single mineral surface (Subrahmanyam *et al.*, 1996). These techniques are slow and non-representative of the flotation mineral particles. Liquid penetration studies, such as equilibrium pressure and wetting rate measurements, are more rapid and reliable techniques for determining the contact angle of minerals. The Washburn technique (wetting rates technique) was used to determine the contact angle. The theory relating to this method is provided in Section 2.2.2.

A clean calibrated glass capillary with a diameter of 2 mm was packed at one end with a thin layer of glass wool to retain the particles. Given that the wetting rate is influenced by the uniformity of the bed, the quartz particles were added to the glass capillary and gently tapped on a plain hard surface while holding the glass capillary vertical to ensure uniform packing.

Figure 3.7 shows the experimental apparatus used for determining the advancing contact angle of quartz particles. The bottom end of the calibrated packed capillary (the end with the glass wool) was introduced to the liquid and rising of the liquid was timed. Water and cyclohexane were used as the non-wetting and wetting liquids, respectively, for determining the contact angle for the hydrophobic quartz.

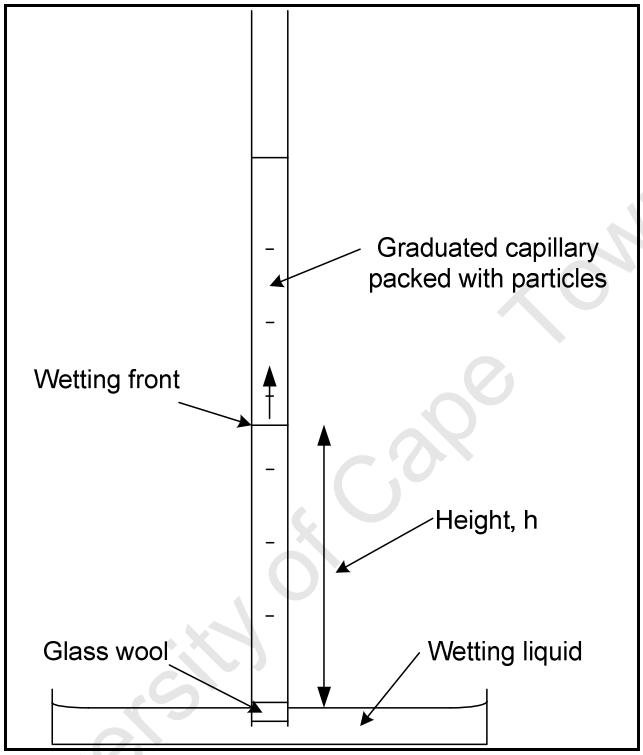

Figure 3.7. Experimental apparatus used for determining the contact angle of particles, as described by Washburn (1921).

A plot of the rise of the water squared (h^2) versus time (t) gives the gradient of the non-wetting liquid and that of cyclohexane gives the gradient of the wetting liquid. Substituting γ_{lv} and η as 72.80 mN/m and 1.0 cP for water and 24.95 mN/m and 0.98 cP for cyclohexane, Equation 2.10 becomes Equation 3.1, which was then used to determine the contact angles.

$$\cos\theta_{nw} = \frac{\text{gradient of non} - \text{wetting liquid}}{\text{gradient of wetting liquid}} \times 0.350 \qquad (3.1)$$

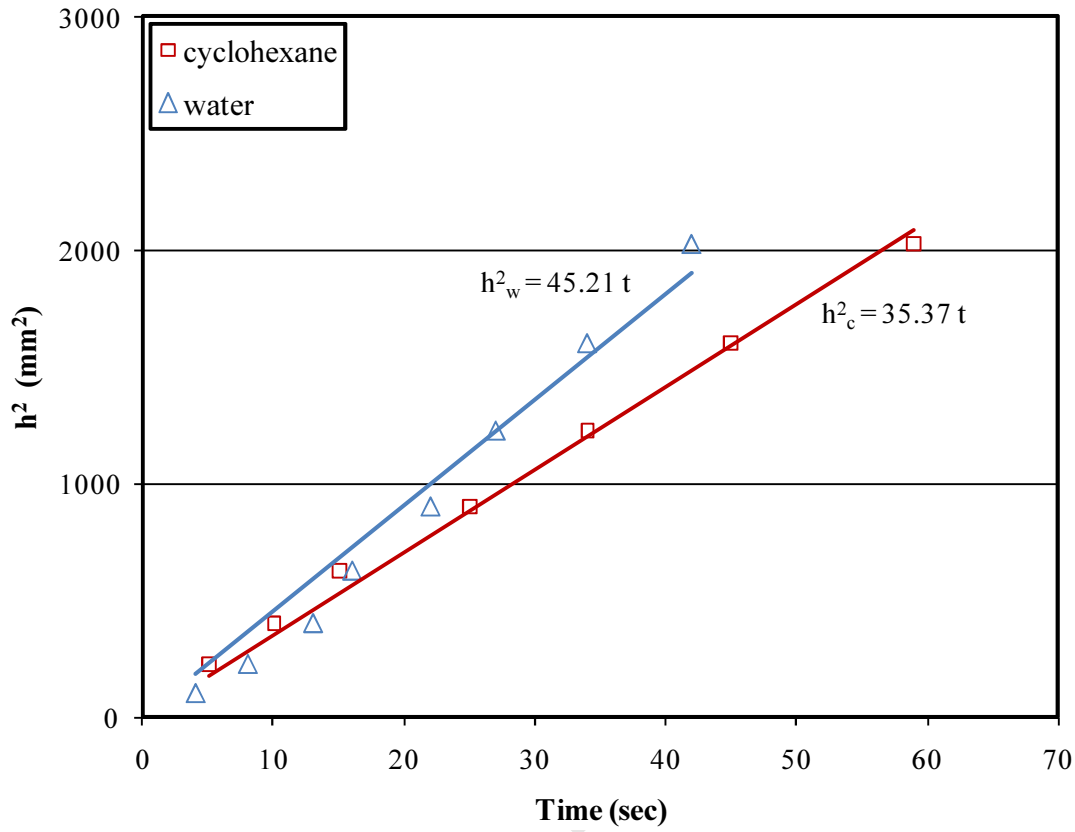

Figure 3.8. Wetting kinetics for -106 µm hydrophobic quartz

The gradients of the non-wetting and wetting liquids were obtained directly from Figure 3.8. In the case of hydrophobic quartz, the wetting liquid (w) is cyclohexane and the non-wetting liquid (nw) is water whereas water is the perfectly wetting liquid and cyclohexane is the non wetting liquid for hydrophilic quartz. The contact angle for the hydrophobic quartz was found to be 65˚, using Equation 3.1, and hydrophilic quartz contact angle was 0˚.

Contact angle tests were done immediately after methylation and two weeks later showed no deterioration in the contact angle measured. Deterioration of the coating during the 10 minutes of flotation was not tested, but was considered very unlikely. Methylated quartz does lose its hydrophobicity due to extended contact with water, but this takes hours/days. Deterioration may also occur as a result of persistent attrition, but this was very unlikely at the low energy levels

and solids concentrations used in the study. Attrition typically requires vigorous stirring at high solids concentrations for extended periods.

3.2.4 Bubble size determination

Bubble sizes were measured photographically by Deglon (1998) by taking photographic images of a stream of aerated fluid removed from the flotation cell and passing it through a flow-through microscope.

In this study, bubbles were generated using sintered glass discs at three different porosities under identical conditions (gas rates, frits, frother type, frother dosage) to those of Deglon (1998). Bubble size was not measured in these experiments, but was measured by Deglon (1998) photographically (the results are given in Table 3.2). The bubbles were too small to be broken up by the grids.

Table 3.2. Mean, Sauter mean and percentile bubble size as measured by Deglon (1998)

	Sparger		
	Porosity 1	**Porosity 3**	**Porosity 4**
d_b (mm)	0.82	0.24	0.13
d_s (mm)	1.05	0.29	0.21
d_{95} (mm)	1.34	0.35	0.28
S_b (/s)	0.05	0.18	0.34

3.3 Flotation experiments

This section details the flotation experimental conditions and procedure of operation. A brief explanation is given for the chosen conditions and then the procedure followed in performing each of the flotation tests. Table 3.3 shows the experimental conditions and variables used in this work.

Table 3.3. The experimental conditions and variables used for the experiments

Experimental conditions	Experimental variables
• Methylated quartz with $\theta = 65°$ • 0.5% solids (mass %) • 100 ml/min N_2 gas • 100 ppm MIBC frother	• d_b = 0.13 mm, 0.24 mm, 0.82 mm • d_p = 80% passing 100 µm • f = 1.8, 4.2, 5.4, 6.4, 7.1 Hz • ε = 0.015 to 0.60 W/kg

3.3.1 Experimental conditions

3.3.1.1 Oscillating amplitude/stroke

A fixed oscillating amplitude equivalent to the grid spacing was used for all the flotation experiments. This allowed all volume elements in the cell to be swept by the grids, which ensured that energy and turbulence were reasonably uniform within the study volume.

3.3.1.2 Choice of reagents

Frother at 100 ppm was added to be consistent with the work of Deglon (2002) and Ahmed and Jameson (1985). This is a high dosage and certainly does eliminate coalescence (CCC ≈ 10 ppm). The bubbles produced were small enough to preclude bubble break-up due to the mixing system (Parthasarathy *et al.*, 1991). Collector was not necessary because the methylated quartz was hydrophobic.

3.3.1.3 Air flow-rate and pulp density

A low constant air flow-rate of 100 ml/min was used for the experiment. Pure nitrogen gas (>99.999%) was passed through a mass flow-meter to four 20 mm diameter gas frits that produced the bubbles. The mass flow controller was calibrated and is quoted to have an accuracy of 0.1%. A very low pulp density of 0.50% was used for the experiment in order to minimise the

effects of entrainment. This is much lower (order of magnitude lower than typical) than would be found in industry or other studies.

Low gas flow-rate and solids concentration were specifically chosen to have minimal influence on the structure of turbulence in the oscillating grid cell, as Bache and Rasool (2001) conducted their measurements in water. The solids concentration of 0.5% m/m (0.2% v/v) was so low that the damping effect of the particles on the turbulence was negligible (Schubert, 1999). At higher air rates (and solids concentrations), turbulence is strongly affected by the presence of both gas and solid phases.

3.3.2 Experimental variables

3.3.2.1 Power input and frequency

The experiments were designed with the primary objective to determine the effect of energy on the flotation process in a nearly ideal system in terms of turbulence and energy dissipation. The effect of energy was investigated by changing the frequency at which the grids oscillated using a variable speed drive. The frequency was converted to specific energy input using Equations 2.65, 2.66 and 2.67 given in section 2.5.3.3. Five different frequency settings were chosen to cover the energy range (0.015 to 0.60 W/kg) being investigated. This is at the lower end of the industry energy range, where collision dominates and detachment is unlikely.

A sample with 80% passing 100 μm, was used for the experiments. It allows investigation of fine particle flotation (sub 10 μm) and the entire particle size range as given in Figure 3.6. Three different bubble sizes (namely 0.13 mm, 0.24 mm and 0.82 mm) were also investigated in order to determine any relationship between bubble size and flotation rate in this hydrodynamic system.

3.3.3 Experimental procedure

Slurry was made up in a glass beaker by stirring 56 g of methylated quartz in deionised water for 4 minutes using a magnetic stirrer. Deionised water was added to the flotation cell with the gas

flowing. This is done to prevent excess water entering the gas frits. The oscillating grids were started and an appropriate amount of MIBC frother was added. A conditioning time of 2 minutes was allowed for the frother before the gas was shut off for 40 seconds to allow the removal of all disseminated gas bubbles in the flotation cell before the solids were added. With the grids still oscillating, the slurry from the glass beaker was added at the top of the cell and allowed to diffuse throughout the cell for 20 seconds. The gas was then turned on at the appropriate flow rate and the stop-watch was started. A suction nozzle connected to a vacuum manifold (cf. Figure 3.5) was skimmed over the surface of the cell to collect four concentrates over an 8 minute period with the tailings being the pulp that remained after the last concentrate was collected. Samples were then filtered, dried and weighed, after which particle size distributions were determined using a Malvern Mastersizer™. The mass of each particle size class in the feed and every concentrate was calculated from this data. The flotation rate constant (k) was then calculated by fitting the standard 1st order rate equation:

$$R(t) = 1 - e^{-kt} \tag{3.2}$$

where the recovery (R) is the fraction of feed recovered at time t.

3.4 Hydrodynamic characterisation of the cell

Bache and Rasool (2001) characterised the cell hydrodynamics in the absence of gas and solids (single phase system), in order to facilitate turbulence measurements, and found the cell to be capable of generating large regions of near homogeneous, isotropic turbulence throughout the vessel.

Figure 3.9 shows the variation of the RMS turbulent velocity through a section of the vessel, as determined by Bache and Rasool (2001). The RMS turbulent velocity has been made dimensionless by dividing by the mean RMS velocity in order to indicate the relative variation i.e. if turbulence in the vessel was perfectly homogeneous this value would be unity throughout. It is clear from this figure that turbulence does vary through the vessel. Here, the coefficient of variation (standard deviation/mean) of the RMS turbulent velocity is 14%. This is trivial in comparison to the magnitude of variation in turbulence in stirred tanks, as reported in numerous studies in the literature (Van't Riet *et al.*, 1976; Schafer *et al.*, 1997; Lee and Yianneskis, 1998;

Newell and Grano, 2006). Stirred tanks have very high levels of turbulence in the impeller region and low turbulence in the bulk vessel. By comparison, the oscillatory multi-grid mixer represents a near ideal hydrodynamic environment for conducting experiments.

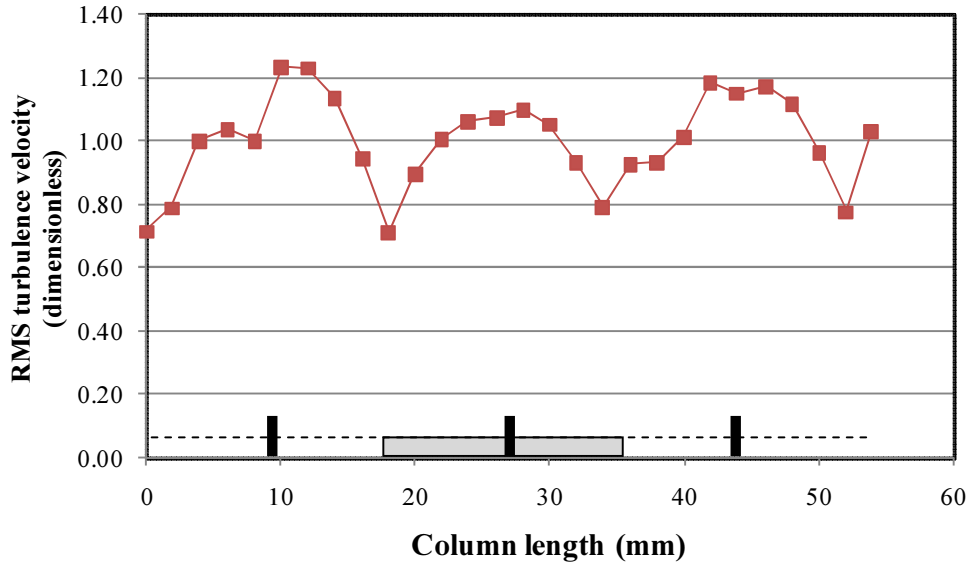

Figure 3.9. Graph of RMS turbulent velocity (dimensionless) versus column height (mm) for a grid frequency of 2.05 Hz. Adapted from Bache and Rasool (2001).

CHAPTER 4 : RESULTS AND DISCUSSION

This chapter presents the results obtained from the flotation experiments performed as well as the relevant discussion. Flotation precharacterisation results are presented in the first section of the chapter. These results show the reproducibility of the rest of the results obtained in this thesis. The section that follows precharacterisation (Section 4.2) takes a look at the effect of particle and bubble size on flotation recovery and flotation rate constant.

In the final section (section 4.3), the findings on the effect of energy on flotation are analysed in detail. This section examines how changes in energy affect flotation for different bubble and particle sizes in this uniform energy regime. In this chapter, emphasis was placed on interpretation of the results compared to the flotation literature.

4.1 Precharacterisation

4.1.1 Flotation recovery

Figure 4.1 shows the relationship between particle size and flotation recovery for the oscillating grid cell at 0.44 W/kg after 8 minutes. The relationship between flotation recovery and particle size is typical for all the energy dissipation rates investigated.

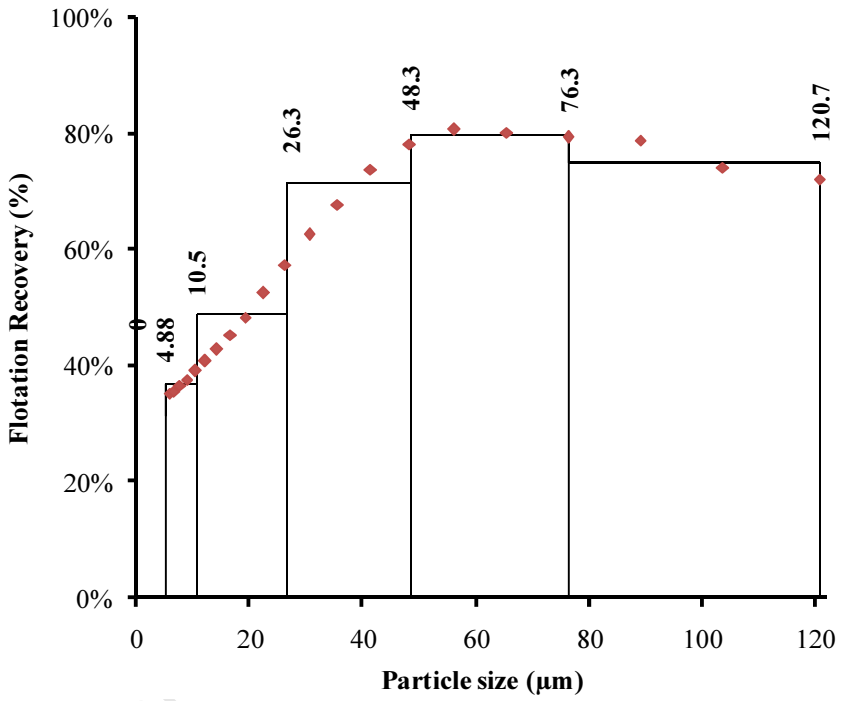

Figure 4.1. Graph showing the relationship between particle size (µm) and recovery (%) for 0.13 mm bubbles after 8 minutes (ε = 0.44 W/kg).

As the particle size increases from 5 µm to 120 µm, flotation recovery increases. This is similar to the findings of numerous researchers (Ahmed and Jameson, 1985; Deglon, 1998; Pyke *et al.*, 2003; Newell and Grano, 2006; Anderson, 2008). The particle sizes investigated in this thesis were grouped into five size classes, as denoted by the blocks in Figure 4.1 based on equal masses of particles in the sub 120 µm region of the flotation feed. The flotation characteristics of ultra-fine particles (0 - 4.88 µm) were not considered in this thesis, because the amount of material recovered in this size class was not appreciable enough for analysis.

4.1.2 Reproducibility

Figure 4.2 shows typical recovery-time curves for two flotation test repeats for fine (-10.5 + 4.9 µm), middling (-48.3 + 26.2 µm) and coarse (-76.3 + 48.3 µm) particles. The curves show that for the three particle sizes, the ultimate recoveries had not been reached after 8 minutes of collection time.

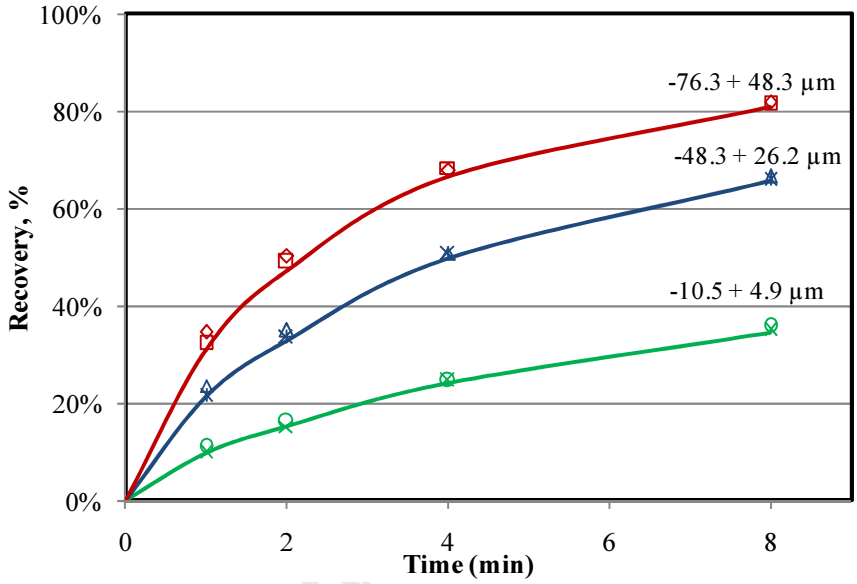

Figure 4.2. Recovery-time curves for three particle size ranges and for three repeat flotation tests (ε = 0.58 W/kg, 0.13 mm bubbles).

All the tests were done in duplicate and the results showed that there was good reproducibility. The error in the recovery increased when propagated to the rate constant resulting in higher errors. Table 4.1 shows relative errors in the recovery and flotation rate constant. Relative errors in flotation rate constants were as high at 5.78% for fine particles and lower for coarse fractions. Errors in the vicinity of less than 5% are acceptable for experimental flotation studies.

Table 4.1 Recovery and rate constants and their relative errors per size class (ε = 0.58 W/kg, 0.13 mm bubbles).

Size fraction	Recovery (8 minutes)	Relative Precision in Recovery	Rate constant (min^{-1})	Relative Precision in Rate constant
4.9 - 10.5 µm	35%	1.64%	0.05	5.78%
10.5 - 26.2 µm	47%	1.58%	0.08	3.72%
26.2 - 48.3 µm	66%	0.76%	0.15	2.51%
48.3 - 76.3 µm	82%	0.25%	0.29	2.25%
76.3 - 120.7 µm	90%	0.14%	0.46	3.20%

4.1.3 Kinetic analysis

4.1.3.1 Modelling

The standard first order flotation rate equation was used to account for the recovery. This model adequately described recovery-time curve behaviour of a single particle size fraction of quartz flotation.

4.1.3.2 Entrainment

The degree of entrainment of material in flotation is commonly assumed to be proportional to the volumetric flow rate of water in the concentrate and a strong function of particle size.

However, gas flow rates were low and therefore water recovery was low. As a consequence, water recovery was 13% compared to 30% obtained by Deglon (1998) and this, coupled with the low solids concentration used, resulted in negligible entrainment. Therefore entrainment was not accounted for.

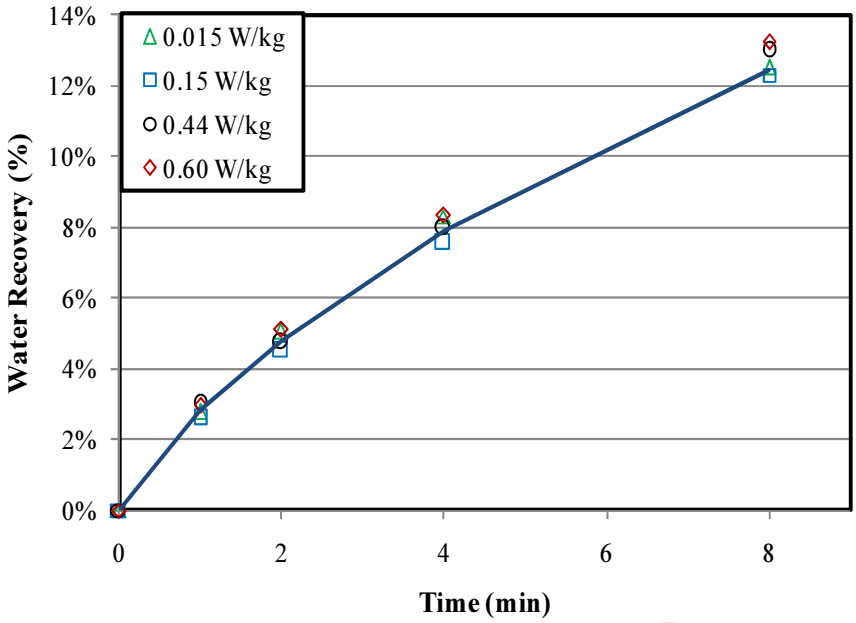

Figure 4.3. Water recovery-time curves for four different energy levels.

Water recovery was also not influenced by energy input, as can be seen in Figure 4.3 above. Turbulence in the oscillating grid cell is homogenous and nearly isotropic, i.e. there is no bulk/convective flow at the pulp-froth interface to influence water recovery.

4.2 Effect of particle and bubble size

This section will consider how flotation is affected by different particle and bubble sizes. The aim of this section is to demonstrate that the effect of particle and bubble size on quartz flotation is typical of that observed by a number of researchers in flotation literature. Flotation rate constant data for all the flotation tests can be found in the Appendix.

4.2.1 Effect of particle size on flotation rate constant

Figure 4.4 and 4.5 show variation of the flotation rate constant with particle size for the three bubble sizes at low and high energy input respectively.

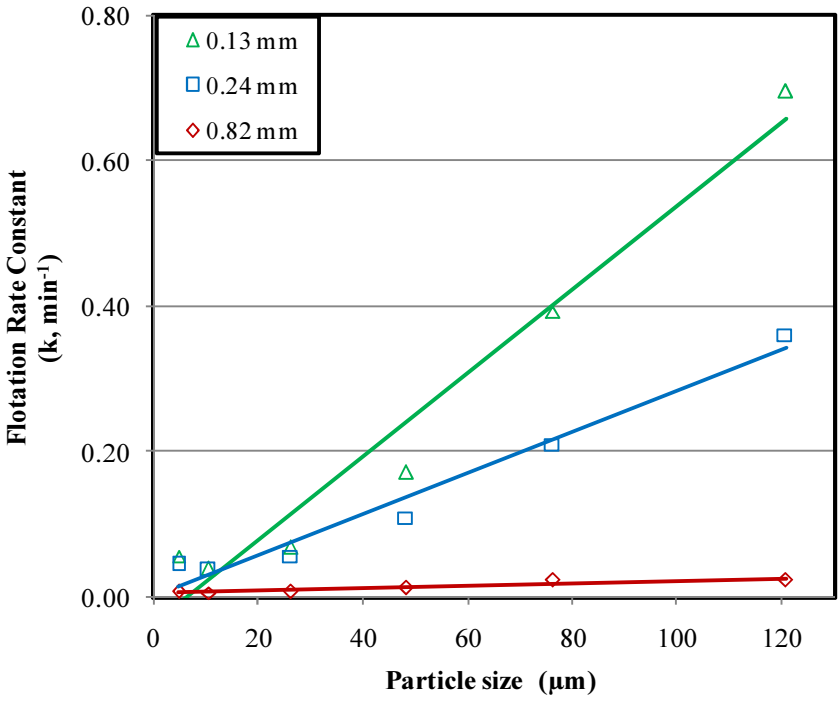

Figure 4.4. Graph of flotation rate constant (min^{-1}) versus particle size (µm) for three bubble sizes (ε = 0.15 W/kg).

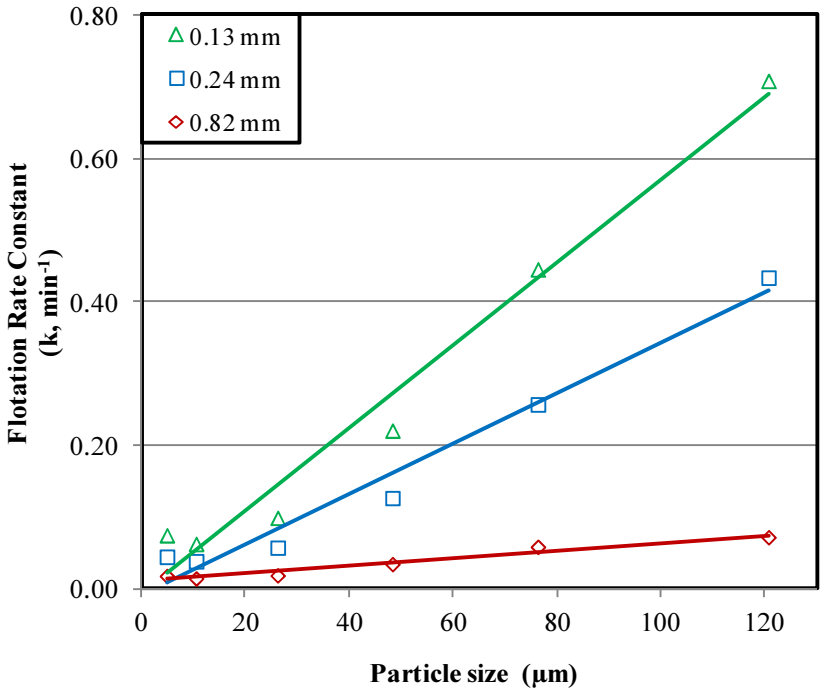

Figure 4.5. Graph of flotation rate constant (min^{-1}) versus particle size (µm) for three bubble sizes (ε = 0.44 W/kg).

Similar trends were observed for the entire energy range (0.015 W/kg – 0.600 W/kg) and therefore the equivalent responses have been omitted. Figure 4.4 and Figure 4.5 show that the relationship between flotation rate constant and particle size is approximately linear for the energy range in this study.

Ahmed and Jameson (1985) and Deglon (1998) found that the flotation rate constant increases gradually with increasing particle size at low impeller speeds (0.08 W/kg and 0.70 W/kg). Deglon (1998), however, found the flotation rate constant to be proportional to particle size to the power 0.15, which is significantly lower than the value of 1.0 found by the author of this thesis. Pyke *et al.* (2003) used a Rushton turbine flotation cell similar to that used by Ahmed and Jameson (1985) and Deglon (1998) and concluded that for particles with moderate to high contact angles, at low turbulent energies (0.10 W/kg and 0.20 W/kg), the flotation rate constant increases almost linearly with particle size based on the collision efficiency model they created. Their experimental data confirmed their findings. Newell and Grano (2006) likewise found a linear relationship between the flotation rate constant and particle size at low superficial gas

velocity for Rushton impeller cells of sizes 2.25 dm^3, 10 dm^3 and 50 dm^3. A number of researchers have found that flotation rate constant for quartz particles increases almost linearly with particle size, at low power intensities (Pyke *et al.*, 2003; Newell and Grano, 2006), as also observed in this work.

4.2.2 Effect of bubble size on the flotation rate constant

Figure 4.6 and Figure 4.7 show variation of the flotation rate constant with bubble size for fine, middling and coarse particle size ranges for low and high energy inputs respectively. The figures show an inverse power relationship between bubble size and the flotation rate constant for all three particle size ranges. Similar trends are observed for all energy settings considered in this study and have therefore been omitted.

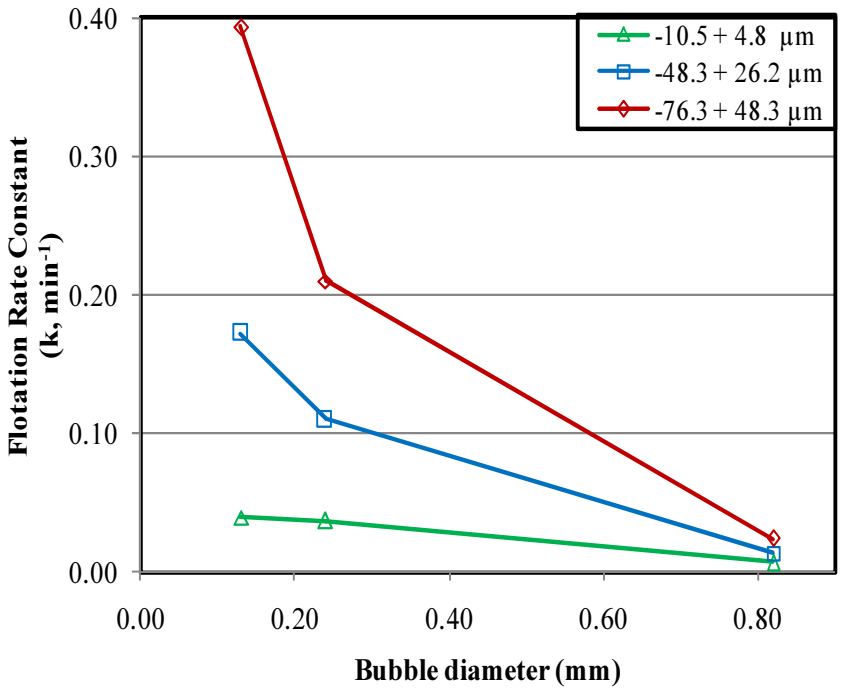

Figure 4.6. Graph of flotation rate constant (min^{-1}) versus bubble size (mm) for three particle size ranges (ε = 0.15 W/kg)

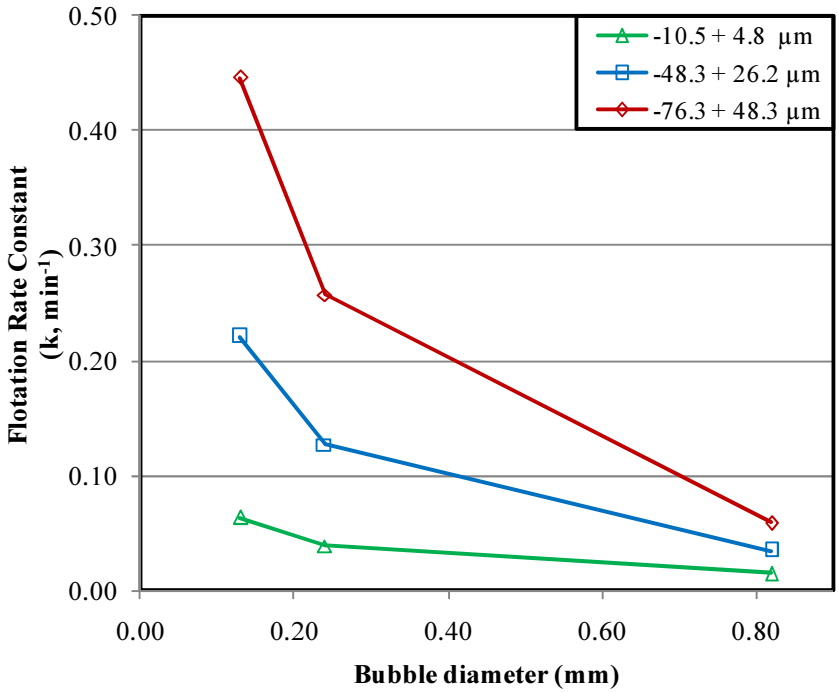

Figure 4.7. Graph of flotation rate constant (min^{-1}) versus bubble size (mm) for three particle size ranges (ε = 0.44 W/kg).

Integrating the work found in literature (Jameson *et al.*, 1977; Ahmed and Jameson, 1985; Yoon and Luttrell, 1989; Deglon, 1998; Pyke *et al.*, 2003; Sherrel and Yoon, 2005; Newell and Grano, 2006) with this study, we can conclude that fine bubbles are better suited for flotation. This inverse power relationship is due to the increased probability of collision for smaller bubbles and this is also well established in flotation literature (Jameson *et al.*, 1977; Yoon and Luttrell, 1989; Sherrel and Yoon, 2005). The flotation rate constant was found to be inversely proportional to bubble size to the power 0.70 – 1.50, with fine particles being proportional to the lower part of this range and large particles being proportional to the higher part of the range.

Reduction in bubble size aids fine particle flotation, but not as significantly as it does for larger particles. Fine particle flotation rate constants remain poor when compared to larger particle flotation rate constants. The inverse relationship between the bubble size and the fine particle flotation rate constant is to the power 0.70 – 0.80, which is lower than the values of between 1.0 and 3.0 reported in literature. This indicates that in nearly ideal hydrodynamic conditions bubble size may not have as significant a role in fine particle flotation.

4.3 Effect of Energy

Energy is known to play a significant role in flotation, especially in the flotation of fine particles. However, most fundamental studies performed to investigate this have been done in complex turbulent systems where energy dissipation varies significantly. In contrast, the oscillating grid cell has uniform energy distribution with homogeneous and nearly isotropic turbulence, making it a more ideal environment in which to perform this study. This section investigates the effect of energy, which is the main objective of this thesis.

4.3.1 Effect of power intensity on the flotation rate constant

Figures 4.8, 4.9 and 4.10 show the relationship between the flotation rate constant and power intensity for the three bubble sizes and for the fine, middling and coarse particle size ranges.

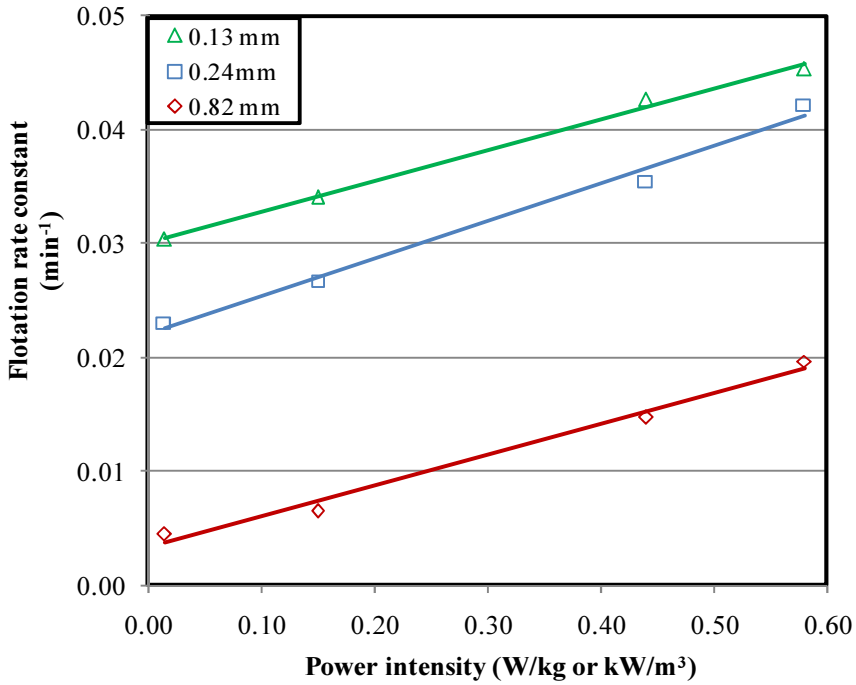

Figure 4.8. Graph of flotation rate constant (min-1) versus power intensity (W/kg) for the -10.5 + 4.9 µm particle size range.

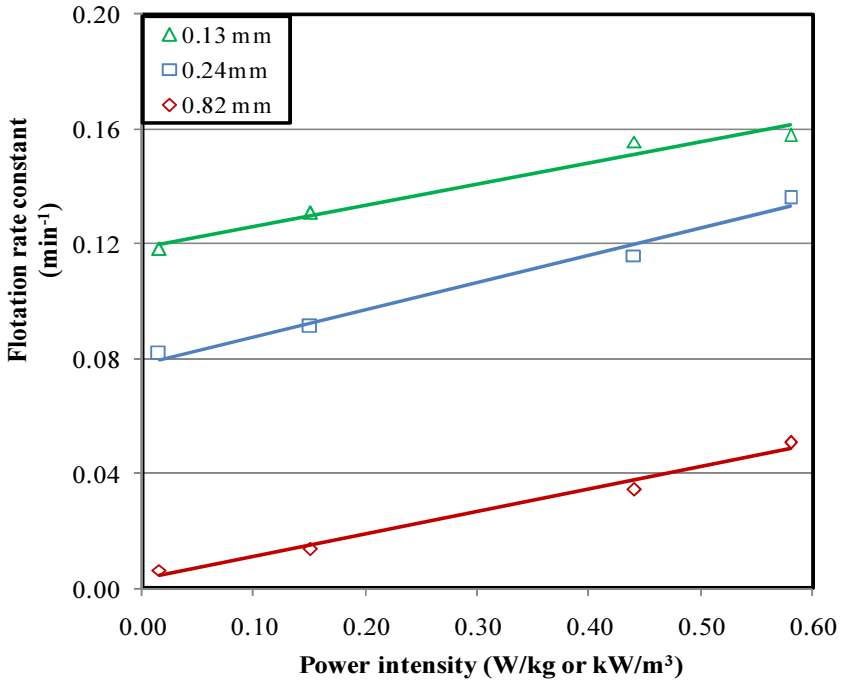

Figure 4.9. Graph of flotation rate constant (min-1) versus power intensity (W/kg) for the -48.3 + 26.2 µm particle size range for different bubble sizes.

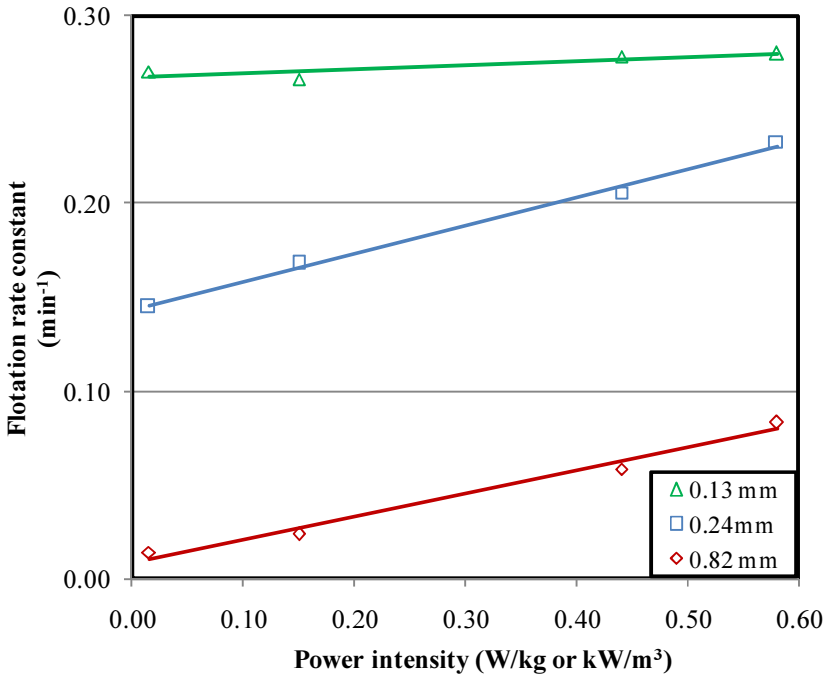

Figure 4.10. Graph of flotation rate constant (min^{-1}) versus power intensity (W/kg) for the -76.3 + 48.3 µm particle size range for different bubble sizes.

Figures 4.8, 4.9 and 4.10 clearly demonstrate that the flotation rate constant increases approximately linearly with increasing power intensity for all particle and bubble sizes. As noted in the literature review, numerous researchers have found that agitation/energy improves the rate of flotation, especially for finer particles. However, the majority of theoretical and experimental studies have found agitation/energy to have less of an effect than the proportional/linear dependence observed in this study. Models for turbulent collision suggest that the rate of flotation is proportional to the specific power input to the power of 0.50 to 0.75. Nonaka *et al.* (1982), Saint Amand (1999) and Deglon (2002) found that the rate of flotation increases with the specific power input to the power of 0.75, 0.50 and 0.91 respectively. However, Newell and Grano (2006) found a linear relationship between the flotation rate constant and specific power input for the flotation of quartz in a stirred tank agitated by a Rushton turbine impeller. This linear relationship was confirmed in a range of geometrically similar flotation cells of volumes 2.25 to 50.0 dm^3.

Figure 4.10 shows a significantly lesser effect of energy on the flotation rate for the 0.13 mm bubbles. These results are for the largest particles and smallest bubbles used in this study. The flotation rate constant remains high, but the effect of energy on the flotation rate constant is not significant. Poor improvement in the flotation rate constant with increasing energy is likely to be an effect of buoyancy and detachment.

4.3.2 Absolute effect of power intensity on the flotation rate constant

Figures 4.8, 4.9 and 4.10 indicate that, for a specific particle size range, increase in the flotation rate constant with increasing power intensity is reasonably similar for the three bubble sizes, even though the magnitudes are different. That is, the flotation rate constants under quiescent conditions (i.e. the intercepts) are very different for the three bubble sizes, but the increase with increasing power intensity (i.e. slope) is reasonably similar. A notable exception is the result for the coarser particle size range with the smallest bubbles, where the increase (i.e. slope) is very slight (cf. Figure 4.10, 0.13 mm). This was generally observed for coarse particles with very small bubbles and is believed to be due to a combination of problems associated with detachment and buoyancy, i.e. the coarse particles are of similar size to the smallest bubbles. Figure 4.11 shows the increase in flotation rate constant with increasing power intensity for all bubble sizes

and for the fine, middling and coarse particle size ranges. The flotation rate constants in this figure are relative to the flotation rate constants under quiescent conditions, i.e. they are obtained by subtracting the intercepts from the flotation rate constants in Figures 4.8, 4.9 and 4.10.

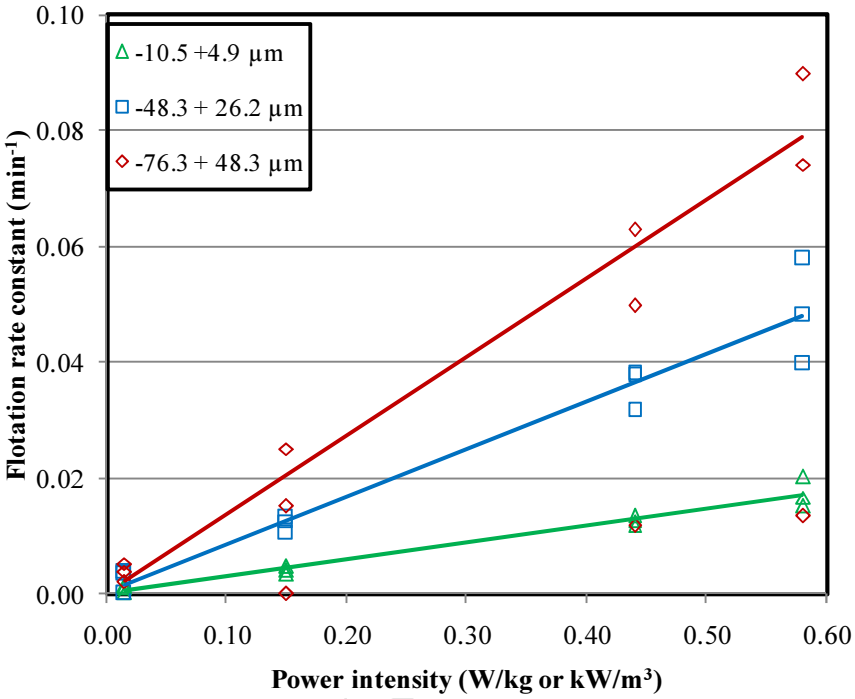

Figure 4.11. Graph showing increase in flotation rate constant (min^{-1}) versus power intensity (W/kg) for three particle size ranges.

There is considerable scatter of the data in Figure 4.11, most notably for the coarse particle size range, where problems associated with small bubbles occur. In particular, the two very low rate constants for the coarse particle size range (<0.02 min^{-1}) correspond to the very smallest bubbles (0.13 mm) at high power intensities and these have been omitted from the trend line. However, it would appear from this figure that the increase in the flotation rate constant with increasing power intensity is a function of particle size, but is less dependent on bubble size. Models for turbulent collision suggest that the rate of flotation is dependent on bubble size (Pyke *et al.*, 2003).

4.3.3 Summary of findings

This study investigated flotation response in an oscillating grid cell using methylated quartz. The cell was proven to have homogenous and nearly isotropic turbulence with uniform energy dissipation (Bache and Rasool, 2001), making it more ideal to investigate the effect of energy on flotation.

Similar to the results obtained previously by other researchers in conventional stirred tanks, the findings in this investigation indicate that energy does indeed increase flotation rates because of increased particle-bubble collision. This study showed that there is a linear relationship between the flotation rate constant and energy for the energy dissipation rate range investigated. This relationship is higher than most found in literature where work was done in stirred tanks. This ties in with the hypothesis that optimal conditions for particle-bubble contacting are lower than those required to produce smaller bubbles (Deglon, 1998).

The oscillating grid cell decouples particle suspension, bubble break-up and particle-bubble contacting, as discussed in chapter 2, contributing to its efficacy for the study of the effect of energy on flotation. Findings in this study suggest that energy input (or agitation) and bubble size may respectively play more and less of a role in promoting particle-bubble contacting in turbulent environments than noted in flotation literature. However, a recent study conducted by Newell and Grano (2006) using a stirred tank also noted this linear dependence.

CHAPTER 5 CONCLUSIONS AND RECOMMENDATIONS

5.1 Conclusions

This study investigated the effect of energy input (or agitation) on the flotation kinetics of methylated quartz particles in a novel oscillating grid flotation cell. Oscillating grids generate near ideal hydrodynamic environments, characterised by turbulence that is relatively homogeneous and isotropic. From this study one may conclude:

Turbulence: The turbulence in the novel oscillating grid cell is more homogeneous and isotropic than in conventional impeller driven flotation cells. At low frequencies, the variance in power intensity is 14%, which is a result of oscillatory flow. This is, however, negligible in comparison to the variance of impeller driven flotation cells.

Particle size: The flotation rate constant increases approximately linearly with increasing particle size and follows an inverse power relationship with bubble size. These trends are well established in flotation literature and consistent for quartz.

Bubble size: There is an inverse relationship between bubble size and flotation rate constant, similar to that found in literature. An increasing inverse power relationship with increasing particle size (4.9 μm – 120 μm) was also observed.

Energy: The flotation rate constant increases approximately linearly with increasing power intensity for all particle and bubble sizes used in this study. The majority of theoretical and experimental studies have found energy input to have less of an effect than the proportional/linear dependence observed in this study, whilst Newell and Grano (2006) also noted linear dependence when using a stirred tank.

Other conclusions were:

- The relative improvement of flotation is observed to be higher for fine particles than for coarse particles.

- The increase in flotation rate constant with increasing power intensity depends on the particle size, but appears to be less dependent on the bubble size.

These findings suggest that energy input (or agitation) and bubble size may respectively play more and less of a role in promoting particle-bubble contacting in turbulent environments than noted in flotation literature.

5.2 Recommendations for future work

Given the findings of this thesis, the following recommendations can be made:

Increased power intensity: Given that this thesis focused on a low energy regime, it is recommended that the oscillating grid cell be tested at higher energy intensity so that is comparable to mechanical flotation cells

Scale up: It is also recommended that a scale up design of the oscillating grind cell be investigated. Section 2.5.3 details the dimensionless numbers that can be used as a basis for scale up.

Other ores: It is recommended that the oscillating grid cell be applied to other ore types to determine its efficacy as flotation device to characterise floatability given that it has homogeneous and nearly isotropic turbulence

REFERENCES

Abrahamson, J. 1975. Collision rates of small particles in a vigorously turbulent fluid. Chemical Engineering Science, 30, pp 1371-1379.

Arbiter, N. 1999. Development and scale-up of large flotation cells. In: Parekh, B. K. & Miller, J.D. (Eds.) Advances in Flotation Technology. Littleton, CO, USA.

Ahmed, N. and Jameson, G.J. 1985. The effect of bubble size on the rate of flotation of fine particles. International Journal of Mineral Processing 14, pp 195-215.

Ahmed, N. and Jameson, G.J. 1989. Flotation kinetics. Mineral Processing and Extractive Metallurgy Review 5, 77–99.

Anderson, C. 2008. Flotation in a Novel Oscillatory Baffled Column. Ph.D thesis, University of Cape Town, Department of Chemical Engineering, Cape Town.

Bache, D.H. and Rasool, E. 1996. Measurement of the energy dissipation around an oscillating grid by an energy balance approach. Chemical Engineering Journal, 63, pp 105-115.

Bache, D.H. and Rasool, E. 2001. Characteristics of turbulence in a multi-grid mixer. Chemical Engineering Journal, 83, pp 67-78.

Bigelow, W.C., Pickett, D.L. and Zisman, W.A. 1946. Oleophobic monolayers, I. Films adsorbed from solution in non-polar liquids. Journal of Colloid Science, 1, pp 1513–538.

Bloom, F. and Heindel, T.J. 2002. On the structure of collision and detachment frequencies in flotation models. Chemical Engineering Science, 57, pp 2467-2473.

Brady, M.R., Telionis, D.P., Vlachos, P.P. and Yoon, R.H. 2006. Velocities of particles and bubbles in grid turbulence measured by particle image velocimetry. International Journal of Mineral Processing, 80 (2-4): pp 133-143.

Breytenbach, J.N. 1995. Investigation of Particle Collection Efficiency in Different Particle Bubble Contacting Environments in Flotation. MSc. thesis, University of Cape Town, Department of Chemical Engineering, Cape Town.

Brunk, B.K., Koch, D.L. and Lion, L.W. 1998. Turbulent coagulation of colloidal particles. Journal of Fluid Mechanics, 364, pp 81-113.

Camp, T.R. and Stein, P. 1943. Velocity gradients and internal work in fluid motion. Journal of the Boston Society of Civil Engineers, 30, pp 219-237.

Chau, T.T. 2009. A review of techniques for measurement of contact angles and their applicability on mineral surfaces. Minerals Engineering, 22, pp 213-219.

Crawford, R. and Ralston, J. 1988. The influence of particle size and contact angle in mineral flotation. International Journal of Mineral Processing, 23, pp 1-24.

Deglon, D.A. 1998. A hydrodynamic investigation of fine particle flotation in a batch flotation cell. Department of Chemical Engineering, University of Cape Town, Cape Town.

Deglon, D.A. 2002. A novel attachment–detachment kinetic model. In: Flotation and Flocculation - From Fundamentals to Applications. Hawaii.

Deglon, D.A. 2005. The effect of agitation on the flotation of platinum ores. Minerals Engineering, 18 (8), pp 839-844.

DeSilva, I.P.D. and Fernando, H.J.S. 1992. Some aspects on mixing in a stratified turbulent patch. Journal of Fluid Mechanics, 240, pp 601-625.

Dickey, T.D. and Mellor, G.L. 1980. Decaying turbulence in neutral and stratified fluids. Journal of Fluid Mechanics, 99, pp 13-31.

Eidelman, A., Elperin, T., Kapusta, A., Kleeorin, N., Krein, A. and Rogachevskii, I. 2002. Oscillating grids turbulence generator for turbulent transport studies. Nonlinear Processes in Geophysics, 9, pp 201–205.

Eidelman, A., Elperin, T., Kleeorin, N., Markovich, A. and Rogachevskii, I. 2006. Experimental detection of turbulent thermal diffusion of aerosols in non-isothermal flows. Nonlin. Processes Geophys, 13, pp 109–117.

Fisher, L.R. 1979. Measurement of small contact angles for sessile drops. Journal of Colloid and Interface Science, 72, pp 200–205.

Hopfinger, E.J. and Toly, J.A. 1976. Spatially decaying turbulence and its relation to mixing across density interfaces. Journal of Fluid Mechanics, 78, pp 155–175.

Jameson, G.J., Nam, S. and Young, M.M. 1977. Physical factors affecting recovery rates in flotation. Miner. Sci. Eng, 9, pp 103.

Janzel, J.G., de Souza, L.B.S. and Schultz, H.E. 2003. Kinetic energy in grid turbulence: Comparison between Data and Theory. J. of the Braz. Soc. of Mech. Sci. and Eng, 4, pp 347-351.

Jordan, C.E. and Spears, D.R. 1990. Evaluation of a turbulent flow model for fine-bubble and fine-particle flotation. Mineral Processing and Extractive Metallurgy Review, 7, pp 65–73.

King, R.P. 1982. Principles of flotation. South African Institute of Minining and Metallurgy. Johannesburg**:** 267.

Kirchberg, H. and Topfer, E. 1965. The mineralization of air bubbles. Proceedings VII. International Mineral Processing Congress. New York.

Kit, E., Strang, E.J. and Fernando, H.J.S. 1997. Measurement of turbulence near shear-free density interfaces. Journal of Fluid Mechanics, 334, pp 293–314.

Koh, P.T.L. and Schwarz, M.P. 2003. CFD modelling of bubble–particle collision rates and efficiencies in a flotation cell. Minerals Engineering, 16 (11), pp 1055–1059.

Kolmogorov, A.N. 1941. Dissipation of energy in a locally isotropic turbulence. Doklady Akad. Nauk SSSR, 32, pp 141.

Kruis, F.E. and Kusters, K.A. 1997. The collision rate of particles in turbulent flow. Chemical Engineering Communications, 158, pp 201-230.

Laskowski, J.S. 1989. Mineral Processing Extractive Metallurgy Rev., 5., pp 25

Lee, C.A. and Erickson, L.E. 1987. Bubble breakup and coalescence in turbulent gas-liquid dispersions. Chemical Engineering Communications, 59, pp 65-84.

Lee, K.C. and Yianneskis, M. 1998. Turbulence properties of the impeller stream of a Rushton turbine. AIChE J., 44, pp 13–24.

Leja, J. and Poling, G.W. 1960. On the interpretation of contact angle. 5th International Mineral Processing Congress IMM, London.

Levins, B.E. and Glastonbury, J.R. 1972. Particle-liquid hydrodynamics and mass transfer in a stirred vessel; Part I - Particle-liquid motion. Chemical Engineering Research and Design, 50, pp 32-41.

Lewis, J.S. 2003. Hydrodynamic effects on the flotation of platinum ore in a pilot flotation plant. MSc thesis. Department of Chemical Engineering, University of Cape Town, Cape Town.

Li, D., FitzPatrick, J.A. and Slattery, C. 1990. Rate of collection of particles by flotation. Industrial Engineering Chemical Research, 29, pp 955–967.

Liepe, F. and Moeckel, H.O. 1976. Studies of the combination of substances in liquid phase. Part 6: The influence of the turbulence on the mass transfer of suspended particles. Chemische Technik, 28 (4), pp 205-209.

Mackenzie, J.M.W. and Matheson, G.H. 1963. Kinetic and dynamic relationships in coal flotation. Transactions Society Mining Engineers, 226, pp 68–75.

Malhotra, D., Hoover, R.M. and Bender, F.N. 1980. Effect of agitation and aeration on flotation of Molybdenite. Mining Engineering, pp 1392–1397.

Matsunaga, N., Sugihara, Y., Komatsu, T. and Masuda, A. 1999. Quantitative properties of oscillating-grid turbulence in a homogeneous fluid. Fluid Dynamics Research, 25, pp 147-165.

McDougall, T.J. 1979. Measurements of turbulence in a zero-mean-shear mixed layer. Journal of Fluid Mechanics, 94 (3), pp 409-431.

Mohamed, M.S. and LaRue, J.C. 1990. The Decay Power Law in Grid Generated Turbulence. Journal of Fluid Mechanics, (219), pp 195–214.

Newell, R. and Grano, S. 2006. Hydrodynamics and scale up in Rushton turbine flotation cells: Part 2. Flotation scale-up for laboratory and pilot cells. International Journal of Mineral Processing, 81, pp 65-78.

Nguyen, A.V., George, P. and Jameson, G.J. 2006. Demonstration of a minimum recovery of nanoparticles by flotation: Theory and experiment. Chemical Engineering Science, 61, pp 2494-2509.

Nonaka, M., Inoue, T. and Imaizumi, T. 1982. A micro-hydrodynamic flotation model and its application to the flotation process. Proceedings XIV International Mineral Processing Congress, Toronto.

Orlins, J.J. and Gulliver, J.S. 2003. Turbulence quantification and sediment resuspension in an oscillating grid chamber. Experiments in Fluids, 34, pp 662 – 677.

Parthasarathy, R., Jameson, G.J. and Ahmed, N. 1991. Bubble breakup in stirred vessels—predicting the Sauter mean diameter. Trans. Inst. Chem. Eng, 69, pp 295-301.

Pyke, B., Fornasiero, D. and Ralston, J. 2003. Bubble–particle heterocoagulation under turbulent conditions. Journal of Colloid and Interface Science, 265 (1), pp 141–151.

Randall, E.W., Goodall, C.M., Fairlamb, P.M., Dold, P.L. and O'Connor, C.T. 1989. A method for measuring bubbles in two- and three- phase systems. Journal of Physics E: Scientific Instruments, 22, pp 827-833.

Ralston, J., Fornasiero, D., Grano, S. R., Duan, J. and Akroyd, T. 2005. Flotation rate constant prediction for metal sulphide particles. Centenary of Flotation Symposium. Brisbane, Australia.

Rotenberg, Y., Boruvka, L. and Neumann, A.W. 1983. Determination of surface tension and contact angle from the shapes of axisymmetric fluid interfaces. Journal of Colloid and Interface Science, 93, pp 169–183.

Saffman, P.G. and Turner, J.S. 1956. On the collision of drops in turbulent clouds. Journal of Fluid Mechanics, 1, pp 16-30.

Saint Amand, J. 1999. Hydrodynamics of deinking flotation. International of Journal Mineral Processing, 56, pp 277–316.

Schafer, M., Hofken, M. and Durst, F. 1997. Detailed LDV measurements for visualization of the flow field within a stirred tank reactor equipped with a Rushton turbine. Trans. Inst. Chem. Eng, 75 (Pt A). pp 729–736.

Schubert, H. and Bischofberger, C. 1978. On the hydrodynamics of flotation machines. International Journal of Mineral Processing, 5, pp 132–142.

Schubert, H.J. 1999. On the turbulence-controlled microprocesses in flotation machines. International Journal of Mineral Processing, 56, pp 257–276.

Schulze, H.J. 1984. Physico-chemical elementary processes in flotation. Elsevier Science Publishers Amsterdam.

Schulz, H.E. and Chaudhry F.H., 1998. A theoretical solution for turbulence generated by oscillating grinds. 15th Brazilian Congress of Mechanical Engineering. SP, Bzazil

Schwarz, S. 2004. The relationship between froth recovery and froth structure. Ph.D. thesis. Ian Wark Reseach Institute, University of South Australia.

Sherrel, I.M. 2004. Development of a flotation rate constant equation from first principles under turbulent flow conditions. Ph.D thesis. Mining and Minerals Engineering, Virginia Polytechnic Institute and State University, Blacksburg.

Sherrel, I. and Yoon, R.H. 2005. Development of a turbulent flotation model. Centenary of Flotation Symposium. Brisbane.

Shy, S.S., Tang, C.Y. and Fann, S.Y. 1997. A nearly isotropic turbulence generated by a pair of vibrating grids. Experimental Thermal and Fluid Science, 14, pp 251-262.

Smoluchowski, M.V. 1917. Versuch einer mathematischen theorie der koagulationskinetik kolloider losungen. Z. Phys. Chem, 92.

Srdic, A., Fernando, H.J.S. and Montenegro, L. 1996. Generation of nearly isotropic turbulence using two oscillating grids. Experiments in Fluids, 20, pp 395-297.

Subrahmanyam, T.V., Prestidge, C.A. and Ralston, J. 1996. Contact angle and surface analysis studies of sphalerite particles. Minerals Engineering, 9 (7), pp 727-741.

Sun, S.C. and Zimmerman, R.E. 1950. The mechanism of coarse coal and mineral froth flotation. Transactions Society Mining Engineers, 187, pp 616–622.

Taggart, A.F., Taylor, T.C. and Ince, C.R. 1930. Experiments with flotation agents. Transactions of the American Institute of Mining and Metallurgical Engineers, 87, pp 285–386.

Tennekes, H. 1975. Journal of Fluid Mechanics, 67 (3), pp 561-567.

Thompson, S.M. and Turner, J. 1975. Mixing across an interface due to turbulence generated by an oscillating grid. Journal of Fluid Mechanics, 67, pp 349–368.

Tsai, C.H. and Lick, W. 1986. A portable device for measuring sediment resuspension. Journal of Great Lakes Res., 12, pp 314-321.

Ura, M., Komatsu, T. and Matsunaga, N. 1987. Entrainment due to oscillating-grid turbulence in two-layered fluid. In: Turbulence Measurements and Flow Modeling. Edited by: C. J. Chen, Chen, L. D. and Holly, F. M. Hemisphere. New York, pp 109-118.

Van't Riet, K., Bruin, W. and Smith, J.M. 1976. Real and pseudo-turbulence in the discharge stream from a Rushton turbine. Chem. Eng. Sci., 31, pp 407–412.

Varbanov, R. 1984. Flotation of spherical particles. Transactions Institute Mining Metallurgy, 93, C6–C8.

Villermaux, E., Sixou, B. and Gagne, Y. 1995. Intense vortical structures in grid-generated turbulence. Physics of Fluids, 7, pp 2008-2013.

Washburn, E.W. 1921. The dynamics of capillary flow. Physical Review 17, 3, pp 273.

Wilhelmy, L. 1863. Annalen der Physik 177.

Williams, J.J.E. and Crane, R.I. 1983. Particle collision rate in turbulent flow. International Journal of Multiphase Flow, 9, 241.

Yoon, R.H. and Luttrell, G.H. 1989. The Effect of Bubble Size on Fine Particle Flotation Mineral Processing and Extractive Metallurgy Review, 5, pp 101 - 122.

Yuu, S. 1984. Rate of small particles in a homogeneous and isotropic turbulence. AIChE Journal, 30 (5), pp 802-807.

APPENDIX

A1: Flotation Recovery Data

Recovery-by-size for 0.13 mm bubbles (Run 1)

Power = 0.015 W/kg										
		Total	Cumulative Recovery (%)							
	Time (min)	Mass (g)	Total	-4.9µm	-10.5 + 4.9µm	-26.2 + 10.5µm	-48.3 + 26.2µm	-76.3 + 48.3µm	-120.7 + 76.3µm	+120.7µm
Conc 1	1	9.38	18.4%	8.4%	6.2%	7.9%	13.9%	20.8%	27.6%	33.3%
Conc 2	2	5.41	29.0%	13.2%	9.9%	12.6%	22.0%	32.8%	43.4%	52.4%
Conc 3	4	6.83	42.3%	20.1%	15.2%	20.0%	34.2%	48.6%	61.9%	71.2%
Conc 4	8	6.18	54.4%	27.6%	21.7%	29.2%	47.4%	63.2%	76.1%	83.6%
Tails		23.27								

Power = 0.15 W/kg										
		Total	Cumulative Recovery (%)							
	Time (min)	Mass (g)	Total	-4.9µm	-10.5 + 4.9µm	-26.2 + 10.5µm	-48.3 + 26.2µm	-76.3 + 48.3µm	-120.7 + 76.3µm	+120.7µm
Conc 1	1	12.87	25.6%	12.1%	9.7%	12.8%	19.4%	28.3%	37.3%	45.1%
Conc 2	2	6.19	37.9%	17.4%	13.7%	18.3%	28.7%	42.8%	56.0%	65.5%
Conc 3	4	6.91	51.6%	25.1%	20.0%	26.9%	42.2%	59.3%	73.6%	82.5%
Conc 4	8	6.09	63.7%	34.0%	28.4%	38.8%	57.0%	73.5%	85.4%	91.4%
Tails		18.26								

Power = 0.44 W/kg										
		Total	Cumulative Recovery (%)							
	Time (min)	Mass (g)	Total	-4.9µm	-10.5 + 4.9µm	-26.2 + 10.5µm	-48.3 + 26.2µm	-76.3 + 48.3µm	-120.7 + 76.3µm	+120.7µm
Conc 1	1	12.88	26.4%	11.1%	8.9%	11.0%	19.9%	30.8%	40.5%	48.1%
Conc 2	2	7.48	41.8%	19.8%	16.6%	21.4%	35.4%	49.2%	60.2%	66.2%
Conc 3	4	6.23	54.6%	25.1%	20.7%	27.0%	45.9%	64.8%	79.5%	86.9%
Conc 4	8	5.13	65.1%	33.1%	29.0%	38.5%	59.1%	77.0%	89.1%	93.3%
Tails		17								

0.60 W/kg										
		Total	Cumulative Recovery (%)							
	Time (min)	Mass (g)	Total	-4.9µm	-10.5 + 4.9µm	-26.2 + 10.5µm	-48.3 + 26.2µm	-76.3 + 48.3µm	-120.7 + 76.3µm	+120.7µm
Conc 1	1	15.26	30.5%	14.1%	11.0%	13.9%	23.7%	34.7%	44.3%	52.5%
Conc 2	2	6.6	43.7%	20.6%	16.2%	20.8%	35.0%	50.2%	62.7%	71.8%
Conc 3	4	7.39	58.4%	30.1%	24.7%	32.4%	50.8%	67.8%	79.7%	86.5%
Conc 4	8	6.28	71.0%	40.9%	35.7%	47.1%	66.5%	81.7%	90.3%	94.0%
Tails		14.54								

Recovery-by-size for 0.13 mm bubbles (Run 2)

Power = 0.015 W/kg										
		Total	Cumulative Recovery (%)							
	Time (min)	Mass (g)	Total	-4.9µm	-10.5 + 4.9µm	-26.2 + 10.5µm	-48.3 + 26.2µm	-76.3 + 48.3µm	-120.7 + 76.3µm	+120.7µm
Conc 1	1	8.29	16.4%	8.2%	6.8%	8.6%	12.5%	17.9%	23.9%	28.7%
Conc 2	2	4.44	25.2%	11.9%	9.7%	12.2%	18.4%	27.6%	37.6%	45.5%
Conc 3	4	5.85	36.8%	17.8%	14.3%	17.8%	27.8%	40.9%	54.2%	64.5%
Conc 4	8	6.03	48.8%	25.1%	20.5%	26.0%	39.6%	54.9%	69.2%	79.1%
Tails		25.82								

Power = 0.15 W/kg										
		Total	Cumulative Recovery (%)							
	Time (min)	Mass (g)	Total	-4.9µm	-10.5 + 4.9µm	-26.2 + 10.5µm	-48.3 + 26.2µm	-76.3 + 48.3µm	-120.7 + 76.3µm	+120.7µm
Conc 1	1	14.32	29.4%	13.4%	11.5%	14.7%	22.7%	33.1%	42.9%	51.0%
Conc 2	2	5.39	40.4%	18.0%	15.2%	19.4%	31.6%	46.2%	59.5%	69.5%
Conc 3	4	6.35	53.4%	24.9%	21.0%	27.4%	44.3%	62.4%	77.1%	84.6%
Conc 4	8	5.18	64.1%	32.1%	27.9%	37.9%	57.7%	75.5%	87.5%	91.4%
Tails		17.52								

Power = 0.44 W/kg										
		Total	Cumulative Recovery (%)							
	Time (min)	Mass (g)	Total	-4.9µm	-10.5 + 4.9µm	-26.2 + 10.5µm	-48.3 + 26.2µm	-76.3 + 48.3µm	-120.7 + 76.3µm	+120.7µm
Conc 1	1	15.04	30.0%	12.3%	9.2%	12.1%	23.3%	35.3%	45.1%	53.7%
Conc 2	2	6.62	43.2%	20.3%	16.4%	22.3%	37.8%	51.5%	60.4%	66.6%
Conc 3	4	7.77	58.8%	27.6%	22.3%	30.4%	51.4%	70.1%	82.3%	89.7%
Conc 4	8	5.51	69.8%	36.4%	31.7%	43.7%	65.8%	82.4%	91.3%	95.7%
Tails		15.15								

0.60 W/kg										
		Total	Cumulative Recovery (%)							
	Time (min)	Mass (g)	Total	-4.9µm	-10.5 + 4.9µm	-26.2 + 10.5µm	-48.3 + 26.2µm	-76.3 + 48.3µm	-120.7 + 76.3µm	+120.7µm
Conc 1	1	14.23	28.0%	12.4%	9.9%	12.2%	21.6%	32.2%	41.3%	48.6%
Conc 2	2	7.18	42.2%	19.1%	15.2%	19.4%	33.5%	48.9%	61.5%	69.8%
Conc 3	4	8.25	58.4%	29.4%	24.6%	32.0%	50.7%	68.4%	80.2%	86.9%
Conc 4	8	6.01	70.2%	39.3%	34.9%	46.0%	65.8%	81.4%	90.1%	93.9%
Tails		15.12								

Recovery-by-size for 0.24 mm bubbles

Power = 0.015 W/kg										
		Total	Cumulative Recovery (%)							
	Time (min)	Mass (g)	Total	-4.9µm	-10.5 + 4.9µm	-26.2 + 10.5µm	-48.3 + 26.2µm	-76.3 + 48.3µm	-120.7 + 76.3µm	+120.7µm
Conc 1	1	12.77	24.3%	12.7%	9.9%	12.7%	20.9%	28.2%	34.5%	39.4%
Conc 2	2	3.76	31.4%	16.0%	12.4%	15.8%	26.6%	36.6%	45.2%	52.2%
Conc 3	4	5.7	42.3%	21.3%	16.8%	21.8%	36.2%	49.4%	60.6%	69.1%
Conc 4	8	5.17	52.1%	27.1%	21.8%	29.0%	46.5%	61.1%	72.5%	80.8%
Tails		25.21								

Power = 0.15 W/kg										
		Total	Cumulative Recovery (%)							
	Time (min)	Mass (g)	Total	-4.9µm	-10.5 + 4.9µm	-26.2 + 10.5µm	-48.3 + 26.2µm	-76.3 + 48.3µm	-120.7 + 76.3µm	+120.7µm
Conc 1	1	12.54	24.6%	12.2%	9.4%	11.7%	20.0%	28.9%	36.2%	40.1%
Conc 2	2	4.07	32.5%	16.1%	12.5%	15.7%	26.8%	38.4%	47.7%	52.6%
Conc 3	4	6.34	44.9%	22.6%	18.0%	23.1%	38.6%	53.1%	64.3%	69.9%
Conc 4	8	5.64	56.0%	29.1%	24.1%	31.5%	50.4%	66.2%	77.3%	82.6%
Tails		22.48								

Power = 0.44 W/kg										
		Total	Cumulative Recovery (%)							
	Time (min)	Mass (g)	Total	-4.9µm	-10.5 + 4.9µm	-26.2 + 10.5µm	-48.3 + 26.2µm	-76.3 + 48.3µm	-120.7 + 76.3µm	+120.7µm
Conc 1	1	12.48	23.8%	11.2%	9.3%	11.6%	19.6%	27.9%	34.5%	39.7%
Conc 2	2	6.02	35.3%	16.7%	13.8%	17.6%	29.7%	41.6%	50.8%	57.1%
Conc 3	4	7.52	49.6%	24.6%	20.8%	26.9%	43.8%	58.6%	69.3%	75.7%
Conc 4	8	6.76	62.5%	32.9%	29.0%	38.2%	58.5%	73.9%	83.4%	87.5%
Tails		19.63								

Power = 0.60 W/kg										
		Total	Cumulative Recovery (%)							
	Time (min)	Mass (g)	Total	-4.9µm	-10.5 + 4.9µm	-26.2 + 10.5µm	-48.3 + 26.2µm	-76.3 + 48.3µm	-120.7 + 76.3µm	+120.7µm
Conc 1	1	11.71	22.4%	10.6%	8.8%	11.5%	18.7%	26.4%	32.4%	36.3%
Conc 2	2	7.33	36.5%	17.4%	14.2%	18.5%	30.6%	43.1%	52.7%	59.0%
Conc 3	4	8.74	53.2%	26.9%	22.9%	30.4%	47.6%	62.7%	73.4%	80.0%
Conc 4	8	7.63	67.9%	37.0%	32.7%	44.7%	65.1%	79.5%	87.9%	92.9%
Tails		16.77								

Recovery-by-size for 0.82 mm bubbles

Power = 0.015 W/kg										
		Total	Cumulative Recovery (%)							
	Time (min)	Mass (g)	Total	-4.9µm	-10.5 + 4.9µm	-26.2 + 10.5µm	-48.3 + 26.2µm	-76.3 + 48.3µm	-120.7 + 76.3µm	+120.7µm
Conc 1	1	2.85	5.6%	3.3%	2.8%	3.4%	5.4%	6.8%	7.7%	7.8%
Conc 2	2.75	0.89	7.4%	4.1%	3.4%	4.2%	6.9%	9.0%	10.4%	10.6%
Conc 3	5	1.35	10.0%	5.9%	4.9%	5.9%	9.4%	12.1%	13.9%	14.1%
Conc 4	8	1.77	13.5%	8.5%	7.3%	8.3%	12.6%	16.1%	18.5%	18.8%
Tails		43.89								

Power = 0.15 W/kg										
		Total	Cumulative Recovery (%)							
	Time (min)	Mass (g)	Total	-4.9µm	-10.5 + 4.9µm	-26.2 + 10.5µm	-48.3 + 26.2µm	-76.3 + 48.3µm	-120.7 + 76.3µm	+120.7µm
Conc 1	1	4	7.7%	4.2%	3.5%	4.4%	7.2%	9.2%	10.7%	11.3%
Conc 2	2	0.75	9.2%	5.0%	4.1%	5.1%	8.5%	11.0%	12.8%	13.5%
Conc 3	4	1.63	12.3%	6.6%	5.4%	6.7%	11.3%	14.8%	17.3%	18.2%
Conc 4	8	3.23	18.6%	10.2%	8.6%	10.7%	17.2%	22.0%	25.6%	27.0%
Tails		42.07								

Power = 0.44 W/kg										
		Total	Cumulative Recovery (%)							
	Time (min)	Mass (g)	Total	-4.9µm	-10.5 + 4.9µm	-26.2 + 10.5µm	-48.3 + 26.2µm	-76.3 + 48.3µm	-120.7 + 76.3µm	+120.7µm
Conc 1	1	5.3	10.4%	5.1%	4.2%	5.3%	8.8%	12.2%	15.1%	16.9%
Conc 2	2	2.23	14.7%	7.3%	6.0%	7.6%	12.6%	17.3%	21.4%	24.0%
Conc 3	4.5	4.31	23.1%	11.7%	9.5%	11.9%	19.9%	27.2%	33.4%	37.7%
Conc 4	8	4.66	32.2%	16.3%	13.4%	17.2%	28.4%	38.1%	46.1%	50.9%
Tails		34.68								

Power = 0.60 W/kg										
		Total	Cumulative Recovery (%)							
	Time (min)	Mass (g)	Total	-4.9µm	-10.5 + 4.9µm	-26.2 + 10.5µm	-48.3 + 26.2µm	-76.3 + 48.3µm	-120.7 + 76.3µm	+120.7µm
Conc 1	1	7.78	14.8%	7.2%	6.0%	8.0%	12.9%	17.4%	21.1%	23.8%
Conc 2	2	2.48	19.5%	9.2%	7.6%	10.2%	16.8%	23.0%	28.1%	31.8%
Conc 3	4	4.54	28.1%	13.3%	11.0%	14.9%	24.6%	33.3%	40.3%	45.2%
Conc 4	8	5.91	39.4%	19.1%	16.3%	22.1%	35.5%	46.4%	55.2%	61.0%
Tails		31.9								

A2: Flotation rate constants (Bubble size = 0.82 mm)

Power	Floatation rate constant (min^{-1}) by particle size					
W/kg	-4.9 µm	-10.5 + 4.9 µm	--26.2 + 10.5 µm	-48.3 + 26.2 µm	-76.3 + 48.3µm	-120.7 + 76.3 µm
0.015	0.0051	0.0045	0.0043	0.0064	0.0143	0.0117
0.15	0.0077	0.0065	0.0077	0.0135	0.0241	0.0239
0.29	0.0148	0.0122	0.0169	0.0307	0.0083	0.0632
0.44	0.0182	0.0147	0.0189	0.0346	0.0587	0.0722
0.58	0.0236	0.0197	0.0282	0.0510	0.0831	0.1039

A3: Flotation rate constants (Bubble size = 0.24 mm)

Power	Floatation rate constant (min^{-1}) by particle size					
W/kg	-4.9 µm	-10.5 + 4.9 µm	--26.2 + 10.5 µm	-48.3 + 26.2 µm	-76.3 + 48.3µm	-120.7 + 76.3 µm
0.015	0.0303	0.0230	0.0343	0.0818	0.1450	0.2263
0.15	0.0338	0.0267	0.0386	0.0912	0.1680	0.2631
0.29	0.0409	0.0345	0.0571	0.1351	0.2648	0.4393
0.44	0.0407	0.0355	0.0519	0.1160	0.2057	0.3056
0.58	0.0486	0.0422	0.0653	0.1358	0.2328	0.3348

A4: Flotation rate constants (Bubble size = 0.13 mm)

Power	Floatation rate constant (min^{-1}) by particle size					
W/kg	-4.9 µm	-10.5 + 4.9 µm	--26.2 + 10.5 µm	-48.3 + 26.2 µm	-76.3 + 48.3µm	-120.7 + 76.3 µm
0.015	0.0414	0.0303	0.0419	0.1180	0.2701	0.4612
0.15	0.0441	0.0340	0.0522	0.1306	0.2663	0.4268
0.44	0.0489	0.0426	0.0695	0.1556	0.2780	0.4010
0.58	0.0522	0.0453	0.0716	0.1578	0.2796	0.4019